Radiogenic Pb mobilization induced by shock metamorphism of zircons in the Apollo 72255 Civet Cat norite clast

Bidong Zhang [a,b,*], Yangting Lin [c], Desmond E. Moser [a], Jialong Hao [c], Yu Liu [d]
Jianchao Zhang [c], Ivan R. Barker [a], Qiuli Li [d], Sean R. Shieh [a], Audrey Bouvier [a,e]

[a] Department of Earth Sciences, The University of Western Ontario, London, Ontario N6A 5B7, Canada
[b] Department of Earth, Planetary and Space Sciences, University of California, Los Angeles, CA 90095-1567, USA
[c] Key Laboratory of Earth and Planetary Physics, Institute of Geology and Geophysics, Chinese Academy of Sciences, Beijing 100029, China
[d] State Key Laboratory of Lithospheric Evolution, Institute of Geology and Geophysics, Chinese Academy of Sciences, Beijing 100029, China
[e] Universität Bayreuth, Bayerisches Geoinstitut, Bayreuth 95447, Germany

Abstract

In situ U-Pb radiometric dating of zircons is regarded as one of the most widely used and reliable methods to acquire geochronologic ages. However, it has been recently reported that radiogenic Pb (Pb*) mobilization within zircon may, in some cases, cause inaccurate age determinations with no geological significance. Such Pb* mobilization can be caused by deformation, α-coil damage, fluid-assisted annealing, and recrystallization. In this study, we report an investigation of Pb* mobilization in shock metamorphosed lunar zircons. NanoSIMS (nanoscale secondary ion mass spectrometry) and IMS 1280HR ion microprobe dating, EBSD (electron backscatter diffraction) and CL (cathodoluminescence) mapping, and scanning ion imaging (SII) were applied to micro-zircon grains from the Apollo 72255 Civet Cat norite clast. Based on the large number of grains with similarities in internal zoning, habit and trace element geochemistry, and host mineral context, the Civet Cat norite zircons are interpreted to be primary, igneous grains. The chronology obtained for three consecutive surfaces (at different depths) by NanoSIMS, SII, and IMS 1280HR, respectively, indicates that the radiogenic Pb distribution of the Civet Cat norite zircons is heterogeneous among different polished or sputtering surfaces. Forty-two NanoSIMS U-Pb ages (beam size of 5 μm) are concordant on a Wetherill Concordia diagram, and their corresponding $^{207}Pb/^{206}Pb$ ages spread from 4015 Ma to 4459 Ma. More notably, the six oldest spots of the 42 define a concordant U-Pb age of 4460 ± 31 Ma (2σ, MSWD = 0.47, P = 0.92) and a weighted mean $^{207}Pb/^{206}Pb$ age of 4453 ± 34 Ma (MSWD = 0.056, P = 0.998). These dates are among the oldest in the lunar highland rocks. However, the $^{207}Pb/^{206}Pb$ ages of repolished surfaces of these zircons by IMS 1280HR (beam size of 5 μm) do not reproduce the NanoSIMS results (up to 300 Ma younger). The SII (spatial resolution of 2 μm) confirms a heterogeneous distribution of radiogenic Pb within single grains. The EBSD mapping of these zircon grains shows that they have 3–20° of cumulative lattice misorientation. It is proposed that shock-related deformation has facilitated Pb* migration after primordial crystallization. With currently available data, we cannot preclude the possibility that the large errors of the U-Pb ages obscure reverse discordance that would bias our oldest $^{207}Pb/^{206}Pb$ ages to older values. Conversely, our data could be explained by mixing of Pb-retention and Pb-loss nanodomains as seen in shocked terrestrial zircon such that U-Pb date of 4460 ± 31 Ma approximates the norite formation.
© 2021 Elsevier Ltd. All rights reserved.

---

* Corresponding author at: Department of Earth, Planetary and Space Sciences, University of California, Los Angeles, CA 90095-1567, USA.

E-mail address: bdzhang@ucla.edu (B. Zhang).

1. INTRODUCTION

The age of solidification of the lunar surface is a critical calibration point for the age estimate for craters, and thereby the bombardment flux, habitability windows and topographic features of inner planets (Morbidelli et al., 2012). Zircon is an ideal mineral for constraining the differentiation of the lunar interior. The occurrence of lunar zircons is associated with residual magmas enriched in K, rare-earth elements, and P (KREEP), and lunar zircons thus crystallized exclusively from KREEP-rich melts (Nemchin et al., 2009a). Additionally, due to the slow diffusion of Pb in zircon (e.g., Lee et al., 1997; Cherniak, 2010), the U-Pb isotope system in the crater floor environment is relatively resistant to later high-temperature Pb loss such as by shock metamorphism in planetary impacts (e.g., Moser et al., 2011). In situ U-Pb dating of lunar zircons by ion microprobes, therefore, has been widely used to constrain the timing of lunar magmatism and crustal formation (e.g., Crow et al., 2016; Hopkins and Mojzsis, 2015; Nemchin et al., 2008; Nemchin et al., 2009a). Nonetheless, the U-Pb isotope systematics can still be disturbed or reset in some extreme conditions (Cherniak, 2010), and at lower temperatures, intra-crystalline radiation damage (metamictization) enables Pb diffusion through lattice defects (Mezger and Krogstad, 1997). It has been recently reported that intracrystalline radiogenic Pb (Pb*) mobilization within zircon may complicate age interpretations. Such Pb* mobilization can be caused by tectonic deformation, α-coil damage, annealing, and fluid-induced recrystallization of zircon crystals (Ge et al., 2019 and references therein). More recently, Pb* mobilization in response to intense shock metamorphism and related heating has also been demonstrated (Arcuri et al., 2020). For lunar geochronology, all the mechanisms must be considered in interpreting ion-microprobe data to obtain precise and accurate formation ages.

Radiogenic Pb (noted Pb*) mobilization has been reported primarily in ancient terrestrial zircons (Ge et al., 2018, 2019; Kusiak et al., 2013a, 2013b, 2015; Peterman et al., 2016; Piazolo et al., 2016; Utsunomiya et al., 2004; Valley et al., 2014; Whitehouse et al., 2014; Williams et al., 1984). The intra-crystalline Pb* mobilization can result in nanometre-scale Pb* clusters to micrometre-scale Pb* enrichment domains. Williams et al. (1984) reported unsupported Pb* causing anomalously old $^{207}Pb/^{206}Pb$ zircon ages in a granodioritic orthogneiss in Antarctica as the first evidence of Pb* mobilization in zircon. The occurrence of nanoscale Pb* enrichment in zircon was first documented in an Archean grain from Jack Hills (Utsunomiya et al., 2004). Micrometre-scale Pb subdomains were later found in some zircon grains from the Napier Complex, East Antarctica, using the scanning ion imaging (SII) technique, and these subdomains have unsupported apparent ages up to 4.2 Ga (Kusiak et al., 2013b). Such Pb* mobilization may also result in Pb nanospheres. These nanospheres may occur as metal Pb (Kusiak et al., 2015; Whitehouse et al., 2017) and Pb oxides (Kusiak et al., 2019) instead of Pb* clusters or domains. The nanospheres usually have anomalously higher $^{207}Pb/^{206}Pb$ ratios and, hence, cause

reverse discordance of U-Pb and Pb-Pb ages (Kusiak et al., 2015). Pb* mobilization is thought to be induced by zircon deformation (Corfu, 2013; Piazolo et al., 2016) and recrystallization (Corfu, 2013; Ge et al., 2018), α-recoil damage (Valley et al., 2014), or thermal annealing (Kusiak et al., 2015). These Pb* enrichment domains and Pb-rich phases are usually smaller than ion-microprobe primary beams and hence may produce in situ $^{207}Pb/^{206}Pb$ dates that are younger or older than the authentic crystallization ages (Kusiak et al., 2013a). The localized Pb* mobilization may produce pseudo-concordant U-Pb ages of ancient zircons due to the mixture of mobilized ancient Pb* and Pb produced by in situ U decay (Ge et al., 2018), and this requires ion-microprobe concordance of ancient zircons to be treated with additional caution. In summary, the intra-crystalline Pb* mobilization and its resultant structures and Pb-rich phases may cause misinterpretation of ion-microprobe U-Pb dates and furthermore can lead to biased conclusions about the authentic crystallization ages of ancient zircons.

For the Moon, the oldest lunar zircon is a mineral clast from the Apollo 72215 breccia and was interpreted to have crystallized at 4417 ± 6 Ma using SIMS Pb-Pb analysis (Nemchin et al., 2009a), whereas the majority of lunar zircon $^{207}Pb/^{206}Pb$ ages peak at $\sim$4.34 Ga (Borg et al., 2015 and references therein). The interpretation of lunar zircon ages and their implication for the timing of lunar primordial magmatism and crustal formation relies on the accuracy and precision of U-Pb dates. Similar to terrestrial zircons, lunar zircons may be subject to the aforementioned Pb* mobilization that compromises the reliability of U-Pb dates by ion microprobes, especially considering lunar zircons have been exposed to ubiquitous shock metamorphism for billions of years. The nanoscale Pb* clustering in lunar zircons was first discovered in a zircon grain within the matrix of Apollo breccia 73235, and the occurrence of Pb* clustering was attributed to impact processes (Blum et al., 2019). Our study presents NanoSIMS (nanoscale secondary ion mass spectrometry) and IMS 1280HR ion microprobe dating, EBSD (electron backscatter diffraction) and CL (cathodoluminescence) mapping, and SII data for a group of igneous zircon grains from the Apollo 72255 Civet Cat norite. We report Pb* heterogeneity within these Civet Cat norite zircons and discuss possible mechanisms of the intra-grain Pb* mobilization.

2. MATERIALS AND METHODS

2.1. Sample description

Sample 72255 is an aphanitic impact melt breccia collected from Boulder 1, Station 2, during the Apollo 17 mission. Boulder 1 is located at the foot of the South Massif in the Taurus-Littrow valley. The boulder may originate from the rim of (or near) the Serenitatis basin but was later deposited on the top of the South Massif (Ryder et al., 1975). The boulder fell from the upper position of the South Massif to the sampling location (Hurwitz and Kring, 2016) about 55 million years ago according to its cosmic-ray exposure age (Leich et al., 1975). It is a polymict breccia

derived from consolidated impact ejecta (Wood, 1975). Notably, this boulder is the source of the Apollo 72215 impact melt breccia (Fig. 1). Apollo 72215 was found to contain a deformed, relatively large (0.5 mm) crystal clast of igneous zircon, which yielded a 150 Ma range of $^{207}Pb/^{206}Pb$ model ages from mostly concordant data. The data were interpreted to result from episodic Pb loss causing a discordant array, the upper intercept of which gave a crystallization age of 4417 ± 6 Ma based on its oldest four $^{207}Pb/^{206}Pb$ ages (Nemchin et al., 2009a).

Aphanitic impact melt breccia 72255 was sampled $\sim$30 cm below breccia 72215 (Fig. 1) and contains diverse lithic clast types (anorthosite-norite-troctolite, anorthosite, devitrified glass, and troctolite) enclosed within a dark-gray to black microbreccia matrix (Schmitt, 1975). The matrix has a medium to high KREEPy content (Nunes and Tatsumoto, 1975). The aphanitic melt components of Apollo 72255 have $^{40}Ar/^{39}Ar$ ages of 3904 ± 16 Ma (80% Ar release) and 3920 ± 16 Ma (50–75% Ar release) (Dalrymple and Ryder, 1996). These Ar-Ar ages have been recalibrated with the revised ^{40}K decay constant (Renne et al., 2011) and the new monitor mineral (MMhb-1) age (Renne et al., 1998). U-Pb ages of zircons separated from sawcuts of the 72255 matrix are as old as 4.4 Ga, peak at 4350 Ma and show a minor cluster at $\sim$4200 Ma (Nemchin et al., 2008). Merrillite and apatite dated within the matrix define an average $^{207}Pb/^{206}Pb$ age of 3925 ± 5 Ma (Thiessen et al., 2017).

We obtained two polished thin sections 72255,123 and 72255,126 (Fig. 2) made from a 2×1.5 cm mafic clast, named the Civet Cat norite, in breccia 72255. The clast is characterized by its relict medium-grained cumulate texture of plagioclase (An_{92-94}) and pyroxene ($En_{72-75}Wo_{2-4}$) (Ryder et al., 1975). The Civet Cat norite is, in considera-
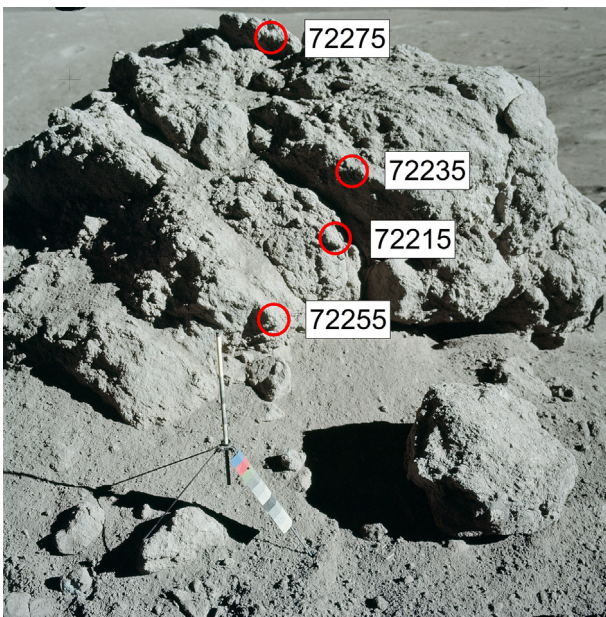

Fig. 1. Photograph of the southeast side of Boulder 1, Station 2, Apollo 17. The circles indicate four sampling positions obtained from Wolfe (1974). Image source: NASA AS17-137-20901.

tion of its microstructure, more properly named a "meta-norite" since the igneous grains have been modified to a granular texture by at least one episode of heating and shock metamorphism. Based on the shock features, it has experienced a shock stage of S3–4 and a peak pressure of 15–35 GPa (Černok et al., 2019). This meta-plutonic rock is believed to have been excavated from the deep crust (10–70 km) (Takeda et al., 1982) and incorporated into the 72255 breccia by later impacts (James, 1983). We interpret the granularization of the once-euhedral grains as due to shock metamorphism, presumably during excavation during complex crater formation. The Rb-Sr radiometric system provides an internal mineral isochron age of 4.16 ± 0.05 Ga (2σ; corrected using the ^{87}Rb decay constant $\lambda = 1.3972 \times 10^{-11}$ yr^{-1} from Villa et al., 2015) for the norite (Compston et al., 1975). The Ar-Ar dating defines a younger age of 3.99 ± 0.03 Ga (Leich et al., 1975) (recalibrated with the ^{40}K decay constant by Renne et al., 2011). The in situ U-Pb dating of apatite gives a similar age of 3930 ± 13 Ma (Thiessen et al., 2017). The relict igneous texture and the chronological studies reporting dates between 4.4 Ga and 3.9 Ga indicate at least a two-stage dynamothermal history for the norite.

2.2. NanoSIMS measurements

Because of the very small size (5–20 μm) and deformed state of the zircon grains in the Civet Cat norite, ultra-high lateral resolution U-Pb dating was required. The NanoSIMS technique was used because its primary beam can reach a lateral resolution of <5 μm (Yang et al., 2012). The NanoSIMS 50L at the Institute of Geology and Geophysics, Chinese Academy of Sciences has seven Faraday cups and seven electron multipliers (EMs), which enable simultaneous analysis of seven isotopic masses. Previous work on igneous lunar zircons from meteorite Sayh al Uhaymir (SaU) 169 showed that the NanoSIMS U-Pb age (3917 ± 17 Ma, 2σ) and Pb-Pb age (3912 ± 14 Ma, 2σ) (Hu et al., 2016) are consistent with those measured by the IMS 1280 (3921 ± 3 Ma, 2σ) (Lin et al., 2012) and sensitive high-resolution ion microprobe (SHRIMP) (3920 ± 13 Ma, 2σ) (Liu et al., 2012).

The detailed method of NanoSIMS U-Pb dating has been previously described in Yang et al. (2012). A summary is provided below. The removal of carbon coating from a large surface can significantly reduce the secondary ion yield. In order to locate the micro-zircons without sputtering too large areas, a dual-beam focused ion beam (FIB) was used to mark all the grains by depositing two vertical Pt bars near the grains before NanoSIMS analyses. With the Pt markers, the small grains of zircon can be accurately located, and the sputtering surface of each spot was reduced to as small as 10×10 μm^2. The same sputtering area size was also applied to reference zircon M257 to maintain 7comparable yield rates of the secondary ions. The primary O$^-$ beam was $\sim$500 pA and optimized by apertures (D0-3 = 100 mm, D1-2 = 300 mm) and lens (L0 = 5.6 kV, L1 = 5.1 kV). The secondary ion species of $^{89}Y^+$, $^{96}Zr^+$, $^{204}Pb^+$, $^{206}Pb^+$, $^{207}Pb^+$, $^{238}U^+$, $^{232}Th^{16}O^+$ and $^{238}U^{16}O_2^+$ were detected. Pb isotopes were detected using the magnetic
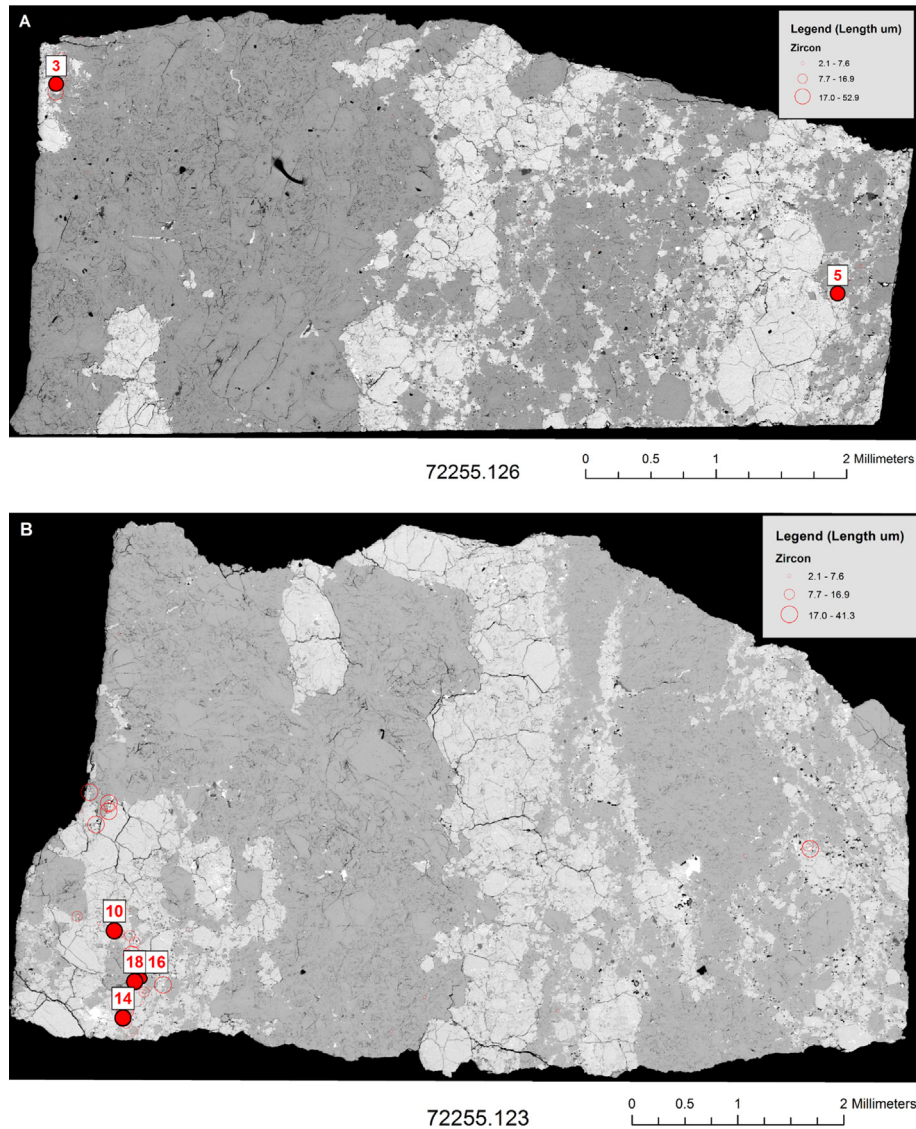
Fig. 2. Scanning electron microscope (BSE) mapping of thin sections 72255,126 (A) and 72255,123 (B). The red dots are the "oldest" zircon grains analyzed in this study (see Section 4.2). The open red circles are other zircon grains. The dark and light gray minerals are plagioclase and pyroxene, respectively. (For interpretation of the references to colour in this figure legend, the reader is referred to the web version of this article.)

peak-switching technique because the short dispersion distance between $^{204}Pb^+$, $^{206}Pb^+$ and $^{207}Pb^+$ allows using only one detector. The Pb isotopes, including a background blank of 203.5 amu, were hence analyzed by magnetic field switching, whereas the other ion species were analyzed at the same time as the ^{206}Pb peak. The mass resolution (M/ΔM, at 10% peak height) was ∼5000. All the mass peaks were centred using reference zircon M257. The power relationship between Pb/U and UO_2/U from M257 was used to calibrate instrumental U-Pb fractionation. M257 has a mean $^{207}Pb/^{206}Pb$ value of 0.0591 ± 0.0040 (2σ, N = 52; Appendices 1 and 2), which is consistent with its reference value of 0.05891 ± 0.00006 (Nasdala et al., 2008). Another two reference zircons, Plešovice and AS3, were measured together with M257. Their concordant U-

Pb ages are 334 ± 6 Ma and 1066 ± 14 Ma (Appendix 3), respectively, which are consistent with their recommended values of 337.13 ± 0.37 Ma (Sláma et al., 2008) and 1099.1 ± 0.5 Ma (Paces and Miller, 1993). The $^{206}Pb/^{204}Pb$ ratios of the Civet Cat norite zircons vary between 739 and 39761, and some are below the detection limit for ^{204}Pb (Table 1). Hence, the isotopic compositions used in correction are not significant to age calculations. Given the highly incompatible nature of Pb in zircon in anhydrous systems (Watson et al., 1997), the $^{206}Pb/^{204}Pb$ variations are attributed to a variable amount of ^{204}Pb incorporated in the sample surface. We see this as having been introduced during the polishing of Apollo thin sections reported by other workers (e.g., Nemchin et al., 2008). This is because the surface of Apollo polished thin sections may be contaminated

Table 1
NanoSIMS U-Pb isotopic ratios and geochemical analysis for zircons from the Apollo 72255 Civet Cat norite.

Sample	Corrected $^{207}Pb/^{206}Pb$	Err (1σ %)	$^{204}Pb/^{206}Pb*$	$^{206}Pb/^{238}U$	Err (1σ %)	U (ppm)	Y (ppm)	Th (ppm)	Th/ U	$^{207}Pb/^{206}Pb$ age (Ma)	± 1σ	$^{206}Pb/^{238}U$ age (Ma)	± 1σ	Dose† (3.93 Ga)	Dose‡ (4.19 Ga)
72255,126															
Z1-1	0.50427	3.50	–	0.9431	2.57	49	579	49	0.98	4254	51	4282	81	1.28	1.46
Z1-2	0.54501	1.58	–	0.9733	2.05	125	770	52	0.41	4368	23	4382	66	3.01	3.47
Z1-3	0.55563	2.18	–	0.9894	2.08	40	625	52	1.29	4396	32	4434	67	1.08	1.24
Z2-1	0.51450	2.45	–	1.0105	2.35	54	555	59	1.09	4283	36	4502	77	1.42	1.63
Z2-2	0.46980	2.66	–	0.9809	2.31	74	610	65	0.88	4149	39	4406	74	1.90	2.18
Z3-1	0.51437	2.60	–	1.0240	3.40	50	474	57	1.14	4283	38	4545	112	1.32	1.52
Z3-2	0.55704	1.84	0.000483	0.9736	2.05	44	501	73	1.66	4400	27	4383	66	1.24	1.42
Z3-3	0.57870	4.13	–	1.0119	2.10	95	711	48	0.51	4455	59	4507	68	2.32	2.67
Z4	0.45994	1.55	–	0.9353	2.61	32	575	73	2.29	4118	23	4257	82	0.97	1.10
Z5-1	0.58028	1.78	0.000594	1.0134	2.09	49	288	116	2.37	4459	26	4511	68	1.50	1.70
Z5-2	0.48058	2.23	0.000583	0.9583	2.12	57	263	86	1.51	4183	33	4333	67	1.58	1.81
Z5-3	0.48505	1.66	0.000291	0.9778	2.05	95	323	92	0.97	4196	24	4396	66	2.46	2.83
72255,123															
Z6	0.53419	2.68	0.000299	0.9812	3.07	94	506	135	1.44	4339	39	4407	99	2.58	2.95
Z7-1	0.48663	2.07	0.000471	0.9607	3.08	180	646	192	1.07	4201	30	4340	98	4.72	5.42
Z7-2	0.55336	3.25	0.000053	1.0085	3.23	185	702	182	0.98	4390	47	4496	105	4.80	5.51
Z8-1	0.48555	1.64	0.000311	0.9329	3.08	137	813	161	1.18	4198	24	4248	97	3.64	4.18
Z8-2	0.48593	1.72	0.000258	0.9787	3.15	81	747	191	2.37	4199	25	4399	101	2.47	2.81
Z8-3	0.46188	0.91	0.000025	1.0314	3.09	106	742	198	1.86	4124	13	4569	102	3.06	3.50
Z9-1	0.45119	2.02	0.000436	0.9354	3.15	34	422	230	6.69	4089	30	4257	99	1.53	1.72
Z9-2	0.46231	3.60	0.000818	0.9064	3.07	32	576	219	6.78	4125	52	4159	95	1.45	1.63
Z9-3	0.48229	2.92	0.000879	1.0204	3.14	38	441	177	4.63	4188	43	4534	103	1.45	1.63
Z9-4	0.42926	2.21	0.000730	0.9150	3.07	31	406	182	5.93	4015	33	4188	95	1.31	1.47
Z10-1	0.52490	2.41	0.000329	1.0451	3.08	53	241	218	4.11	4313	35	4612	102	1.93	2.17
Z10-2	0.57534	3.92	0.000053	0.9678	3.13	28	176	188	6.71	4447	56	4364	100	1.26	1.41
Z10-3	0.54530	2.81	0.000529	1.0529	3.99	58	202	150	2.59	4369	41	4637	133	1.81	2.06
Z10-4	0.44260	2.28	0.000439	0.8678	3.23	61	345	136	2.23	4061	34	4028	98	1.84	2.09
Z11-1	0.46961	1.35	0.000053	0.9049	3.12	69	312	196	2.83	4149	20	4154	96	2.22	2.52
Z11-2	0.43724	2.72	0.000053	0.8286	3.18	125	329	117	0.93	4042	40	3891	94	3.23	3.70
Z12-1	0.49323	2.71	0.001251	1.0469	4.04	23	242	190	8.07	4221	40	4618	134	1.15	1.29
Z12-2	0.53812	1.81	–	1.0407	3.11	50	242	193	3.86	4349	26	4598	103	1.78	2.01
Z13	0.53289	3.50	0.000700	0.9585	3.48	57	263	222	3.90	4335	50	4333	111	2.03	2.29
Z14-1	0.57757	3.25	0.000907	1.0581	3.47	26	184	200	7.69	4453	47	4653	116	1.25	1.40
Z14-2	0.55662	3.17	0.001092	0.9954	3.46	28	203	187	6.68	4399	46	4453	112	1.26	1.41
Z15	0.48033	6.98	0.001359	0.9151	3.08	60	261	217	3.62	4182	100	4189	96	2.08	2.36

Table 1 (*Continued*)

Z16	0.57907	4.77	–	3.07	0.9901	52	259	162	3.12	4456	68	4436	99	1.72	1.95
Z17	0.48192	2.60	0.000449	3.73	0.9731	27	220	169	6.19	4187	38	4381	120	1.17	1.32
Z18-1	0.50403	4.15	0.000861	3.10	0.8790	40	231	224	5.60	4253	60	4066	94	1.65	1.85
Z18-2	0.56975	3.11	–	3.51	1.0036	25	194	157	5.28	4433	45	4480	114	1.09	1.22
Z19	0.50052	1.90	0.000410	3.07	0.9153	75	239	192	2.55	4243	28	4189	95	2.34	2.66
Z20	0.56475	4.02	0.000170	3.10	1.0232	51	333	222	4.38	4420	58	4543	102	1.89	2.14
Z21-1	0.49783	1.06	0.000186	3.11	0.9523	209	754	165	0.79	4235	16	4313	98	5.32	6.08
Z21-2	0.52148	2.31	0.000278	3.09	1.0054	202	717	186	0.92	4303	34	4486	101	5.20	5.97

* "–" means that the $^{204}Pb/^{206}Pb$ ratios are below the detection limit for ^{204}Pb.

† and ‡ are the accumulated α-decay doses since 3.92 Ga and 4.19 Ga, respectively, and the unit is 10^{15} events/mg.

by terrestrial common Pb during polishing, and this process primarily introduced common Pb to the Apollo zircons (Nemchin et al., 2008). Therefore, all $^{207}Pb/^{206}Pb$ ratios were corrected from using the modern common Pb composition from the Stacey-Kramers model (Stacey and Kramers, 1975). A possible contribution of inherited lunar common Pb was not considered owing to uncertainties on the lunar U/Pb evolution (Connelly and Bizzarro, 2016) and the expected minimal contribution of initial Pb due to its very high incompatibility in zircon (Watson et al., 1997).

A similar instrumental configuration was applied to the trace-element (including Ti, P, Y, and REE) analyses. The method is described in Hao et al. (2016). Due to the limited number and small size of the zircon grains, trace-element analyses were made in the same pits (less than 1 μm deep) from the former NanoSIMS U-Pb dating. To get a sufficient intensity of light REE (LREE), the beam current was elevated to ~1 nA. To reduce the interference of LREE monoxides to HREE (heavy REE), a high mass resolution of 10,000 (M/ΔM, at 10% peak height) was used, and the entrance slit, aperture slit and exit slit were adjusted to 10 μm, 80 μm and 90 μm, respectively. The first analytical session included ^{49}Ti, ^{89}Y, ^{96}Zr, ^{151}Eu, ^{165}Ho, and ^{175}Lu (Appendix 4). The second had ^{31}P, ^{89}Y, ^{96}Zr, ^{141}Pr, ^{157}Gd, and ^{173}Yb. The high-concentration Y was compared between the two sessions to ensure that the same pits were sputtered. Reference zircon M257 was selected to calibrate the trace-element analyses. U, Th, and Y concentrations of M257 used for the trace-element calibrations are 840 ppm, 226 ppm, and 150 ppm, respectively (Nasdala et al., 2008).

2.3. IMS 1280HR measurements

After the NanoSIMS analytical sessions, the surface of thin section 72255,126 was repolished by neutral solution and colloidal 0.05-μm alumina polish for 20 min. We used the IMS 1280HR at the Institute of Geology and Geophysics, Chinese Academy of Sciences to image and reanalyze the same zircons. Prior to imaging and dating, the thin section was coated with gold. The target spots were less than 5 μm from each other within one zircon grain, so only Pb-Pb dating was performed to avoid fractionation changes of U and Pb due to the different conductive conditions of the sample surface during IMS 1280 analyses (Liu et al., 2020a). The detailed methods of 5-μm-scale monocollector mode Pb-Pb dating were described in Li et al. (2009), Liu et al. (2011, 2020b), and Zhou et al. (2013).

For the IMS 1280 SII procedures, the target area was first pre-sputtered using a ~10 nA $^{16}O^-$ Gaussian illumination primary beam (25 μm) rastering for 2 minutes to remove the gold coating and superficial contamination. A 200 pA $^{16}O^-$ primary beam with a beam size of ~2 μm was used to acquire SII images in a $20 \times 20\ \mu m^2$ area. The field aperture and entrance slit were opened to 6000 μm and 60 μm, respectively. The nuclear magnetic resonance (NMR) magnet controller was used to stabilize the magnet. The oxygen flooding technique was introduced to improve Pb^+ ion yield, hence analytical precision (Li et al., 2009). The secondary ion species of $^{180}Hf^{16}O$,

^{204}Pb, ^{206}Pb, and ^{207}Pb were measured by four multi-collector EMs operated at a mass resolution (M/ΔM) of ~8000 (50% peak height). All species have an integration time of 30 seconds for 100 cycles. The accumulation of all cycles, calculation of ^{207}Pb/^{206}Pb ratios, and age determination of ROIs (regions of interest) were performed using the CAMECA WinImage II program. All the ROI ^{207}Pb/^{206}Pb ratios were corrected by the internal fractionation factor of 1.033962 derived from the measurement of reference zircon M257.

For the Pb-Pb dating, the Gaussian illumination ^{16}O$^-$ primary beam reached a lateral resolution of 5 μm. Oxygen flooding was also applied. The analytical spots were pre-sputtered using a ~6 nA beam for 100 seconds in a 25 × 25 μm^2 area to clean the gold coating and surface contamination. The primary beam was 400–800 pA. The secondary ion species of ^{180}Hf^{16}O, ^{94}Zr$_2$^{16}O$_2$, ^{204}Pb, ^{206}Pb, and ^{207}Pb were detected by a single EM detector using the peak-jumping mode. The mass resolution (M/ΔM) was at ~7000 (50% peak height). ^{180}Hf^{16}O, ^{94}Zr$_2$^{16}O$_2$, ^{204}Pb, ^{206}Pb, and ^{207}Pb had an integration time of 0.48 s, 0.32 s, 8 s, 4 s, and 10 s, respectively. All the mass peaks were calibrated using reference zircon M257. The ^{180}Hf^{16}O peak was used to centre the secondary beam and mass position adjustment before each analysis. Each analysis consisted of 8 cycles and lasted for ~10 minutes. The common Pb correction followed the same procedure as the NanoSIMS results (Section 2.2).

2.4. Electron backscatter diffraction (EBSD) and cathodoluminescence (CL)

The scanning electron microscope (SEM)-EBSD mapping and SEM-CL imaging were performed in the Zircon and Accessory Phase Laboratory at the University of Western Ontario using Hitachi SU6600 VP-FEGSEM equipped with a Gatan Chroma CL detector and an Oxford Instruments Nordlys EBSD detector. The thin sections were imaged in a flat orientation for CL and re-mounted in a 70° pre-tilt holder for EBSD with a working distance of 19 mm. The CL and EBSD detectors were operated by accelerating voltages of 10 kV and 20 kV, respectively. The collection time of electron backscatter diffraction pat-

terns (EBSP) was 55 ms per frame. Frame averaging of 4, binning of 4 × 4, and high gain were used to increase the signal to noise ratios for individual EBSP. Between 6 and 8 bands were used to index EBSPs via a Hough resolution of 60. Automated EBSD mapping results of phase, crystallographic orientation, and EBSP strength were analyzed using Oxford HKL Channel 5 software.

3. RESULTS

3.1. Petrology of the Civet Cat norite thin sections

The mesostructure of the norite in thin sections 72255,123 and 72255,126 is defined by a melanocratic matrix (pyroxene) and discontinuous, cm-scale leucocratic (plagioclase) domains, the latter forming streaks and patches interpreted as a relict cumulate texture (Fig. 2). The pyroxene matrix consists of anhedral pyroxene grains (20–500 μm), which in the thin section exhibit exsolution domains of green and brown phases (possibly ilmenite or chromite) along cleavage planes (Fig. 3A). Large plagioclase grains (>1 mm) make up as much as 40 vol.% of the clast. Plastic deformation (kink banding) is a common feature of the plagioclase, some of which has partially transformed into diaplectic glass (Fig. 3B). The accessory minerals include zircon, apatite, baddeleyite, ilmenite, kamacite, and troilite. More than two dozen micro-zircon grains (<20 μm) were found in the two thin sections, most with anhedral form. These zircons occur most often at the boundaries of plagioclase and pyroxene grains (Figs. 2 and 4).

3.2. SIMS U-Pb ages

3.2.1. NanoSIMS

For sections 72255,123 and 72255,126, the U-Pb isotopic compositions of 20 micro-zircon grains at 42 spots were analyzed by NanoSIMS (Table 1). The U-Pb ages of the 42 spots are concordant on the Wetherill diagram (Fig. 5A), and the associated ^{207}Pb/^{206}Pb model ages range from 4015 ± 33 Ma (1σ) to 4459 ± 26 Ma (Table 1), which are mostly concordant with the U-Pb ages on the Tera-Wasserburg diagram (Fig. 5B).
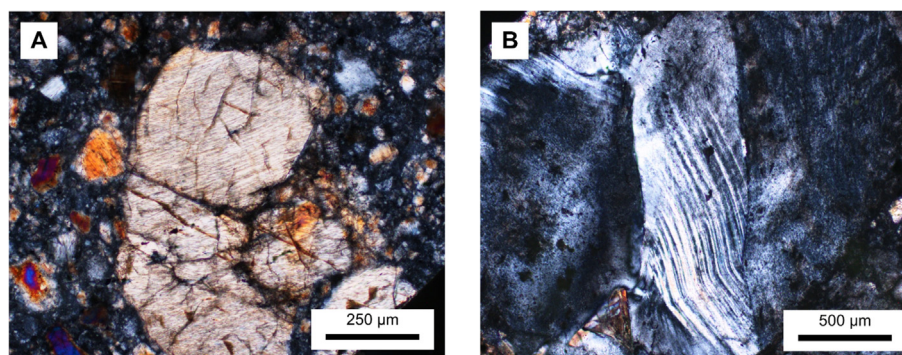

Fig. 3. Orthopyroxene (A) and anorthite (B) grains from the Civet Cat norite under crossed polarized light. The orthopyroxene grains have irregular fractures and exsolved phases along cleavage. The anorthite grains exhibit kink bands and are partially transformed into diaplectic glass.
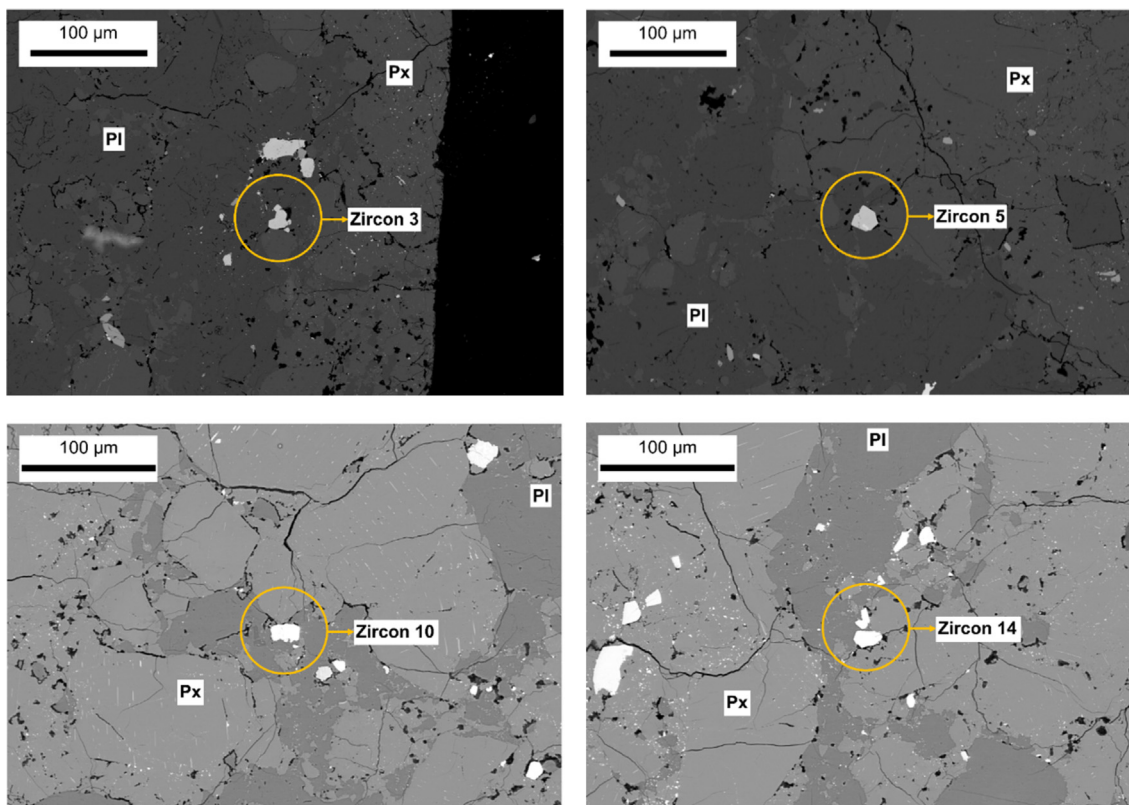
Fig. 4. Petrological context of selected zircon grains in BSE images. Px and Pl denote pyroxene and plagioclase, respectively.

3.2.2. IMS 1280HR

To examine Pb distribution within these zircons in the plane of section, thin section 72255,126 was repolished, and Pb-Pb dating was performed by IMS 1280HR on zircons 1, 3, and 5. These three zircon grains have typical igneous features (igneous growth zoning and crystal facets) and ancient domains previously measured by NanoSIMS: Z1-3 (4396 ± 32 Ma, 1σ), Z3-2 (4400 ± 27 Ma), Z3-3 (4455 ± 59 Ma), and Z5-1 (4459 ± 26 Ma). The IMS 1280HR ^{207}Pb/^{206}Pb model ages are younger, ranging from 4113 ± 13 Ma (1σ) to 4393 ± 12 Ma. The IMS 1280HR ages have smaller analytical uncertainties (Table 2) compared with the NanoSIMS results (Table 1), but their uncertainties are slightly higher than those of typical ion-microprobe measurements for lunar zircons (e.g., Crow et al., 2016; Grange et al., 2009; 2011; Meyer et al., 1996; Nemchin et al., 2008, 2009a, 2009b). The ^{207}Pb/^{206}Pb ages of the same analytical locations by IMS 1280HR on a different surface do not reproduce the NanoSIMS results, except for Z3-1, Z5-2, and Z5-3 (Table 2). The age difference between these two analytical sessions varies between 139 Ma and 346 Ma (excluding errors). One cycle in each of the analytical runs of both Z1R-2 and Z3R-4 showed a spike of ^{207}Pb/^{206}Pb ratios among their eight measurement cycles.

3.3. Zircon REE distribution

U, Th, Y, and REE (Pr, Eu, Gd, Ho, Yb, and Lu) concentrations of the Civet Cat norite zircons were analyzed in order to compare within the population of grains to help understand the behaviour of the U-Pb system. The Y concentrations range from 176 ppm to 711 ppm (mean = 306 ± 149, 1SD; Table 1), and U and Th concentrations range from 26 ppm to 95 ppm (mean = 51 ± 22) and from 48 ppm to 218 ppm (mean = 140 ± 58), respectively. Zircons of thin section 72255,126 have lower Th/U ratios (0.51–2.37) than those of 72255,123 (2.23–7.69). The six "oldest" subdomains have relatively higher Th concentrations (Table 1), and the highest Th/U is 7.69 from Z14-1 (4453 ± 47 Ma).

All REE concentrations for the analyzed zircons from section 72255,123 are listed in Appendix 4, and CI chondrite-normalized REE patterns are plotted in Fig. 6. Overall, the patterns of REE have similarly steep slopes. Compared with HREE (Ho, Yb, and Lu), the LREE (Pr, Eu, and Gd) have lower concentrations, and their concentrations vary much more. Pr has concentrations from 0.01 ppm to 0.19 ppm; Eu from 0.09 ppm to 0.38 ppm; Gd from 1.32 ppm to 8.20 ppm. The concentrations of HREE are more homogeneous: Ho = 7.86 ± 1.34 ppm, Yb = 49.19 ± 9.37 ppm, and Lu = 11.80 ± 2.07 ppm (1SD). The similar REE patterns and HREE concentrations of these grains are consistent with a common, igneous origin for the population.

3.4. Zircon microstructures

The microstructures and deformation features of the zircons were investigated by CL imaging and EBSD mapping
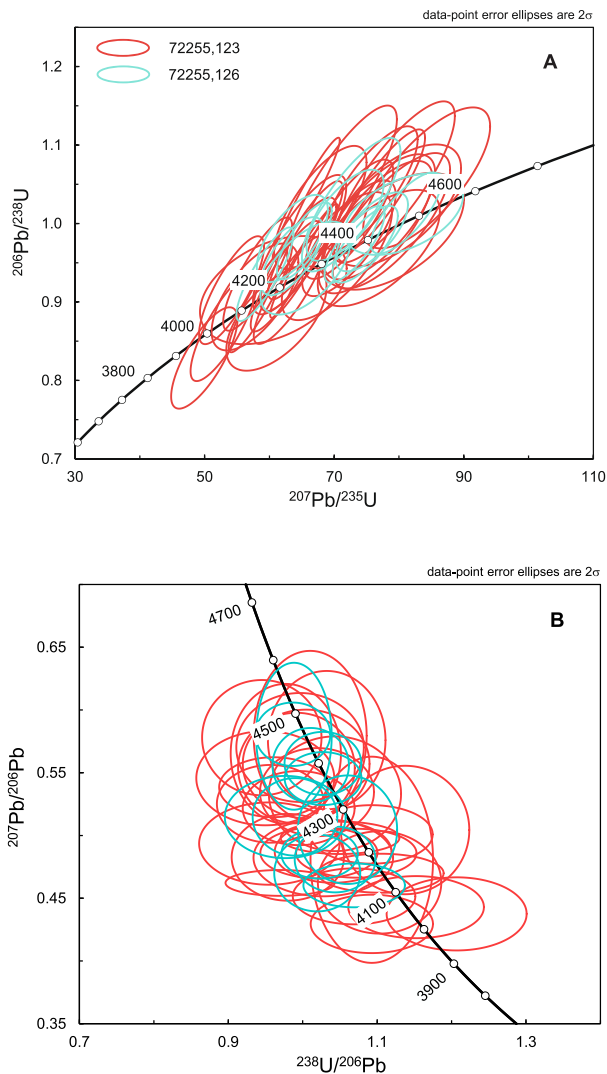
Fig. 5. Concordia diagram of all the zircon in thin sections 72255,123 and 72255,126 dated by NanoSIMS. A: Wetherill Concordia diagram; B: Tera-Wasserburg Concordia diagram. Red and blue legends denote the 72255,123 and 72255,126 zircons, respectively. All ellipses are plotted in 2σ.
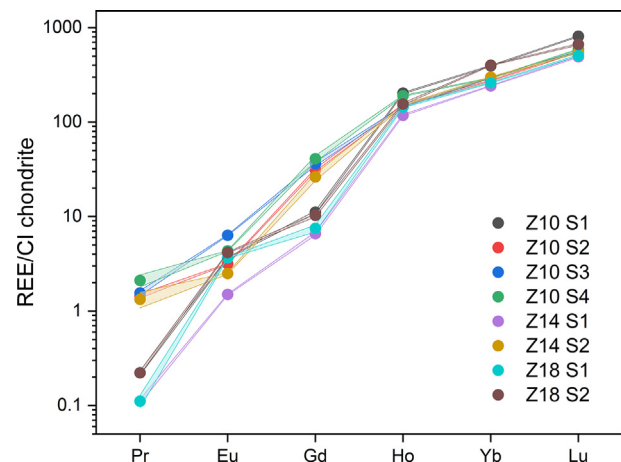

Fig. 6. CI chondrite-normalized REE patterns of selected zircon grains from thin section 72255,123. The CI chondrite composition is from McDonough and Sun (1995).

to assess zircon paragenesis and deformation history. The positions and contexts of the zircon grains in 72255,123 and 72255,126 are shown in Fig. 2. Chemical and orientation microstructural analyses of the zircons reveal relict primary igneous features as well as modification of grain morphology and crystallographic orientation by at least one generation of deformation. Primary features include crystal facets parallel to concentric trace-element zoning typical of igneous zircons (Corfu et al., 2003). The facets are exhibited best by zircon grains Z3 and Z5 (Fig. 7). Zircon Z3 exhibits four crystal facets in a "hopper" form. Although the crystal facets of Z5 are less visible than those of Z3, the partial core of both grains can be seen in the CL images (Fig. 7F and 7K). Z1 has primary oscillatory zoning shown in the CL image (Fig. 7A). The EBSD crystallographic orientation mapping also reveals at least 3–7° cumulative misorientation across all zircons (examples shown in Fig. 7). In some grains, the cumulative misorientation can reach up to 10° (Z1 and Z10) and 20° (Z9). EBSD mapping shows that Z1 and Z2 have shock-related micro-twin structures (Fig. 7B). Shock-induced micro-

Table 2
SIMS 1280HR Pb-Pb isotopic ratios and ages for the Apollo 72255,126 zircons. The NanoSIMS ages of corresponding spots are listed for comparison purposes.

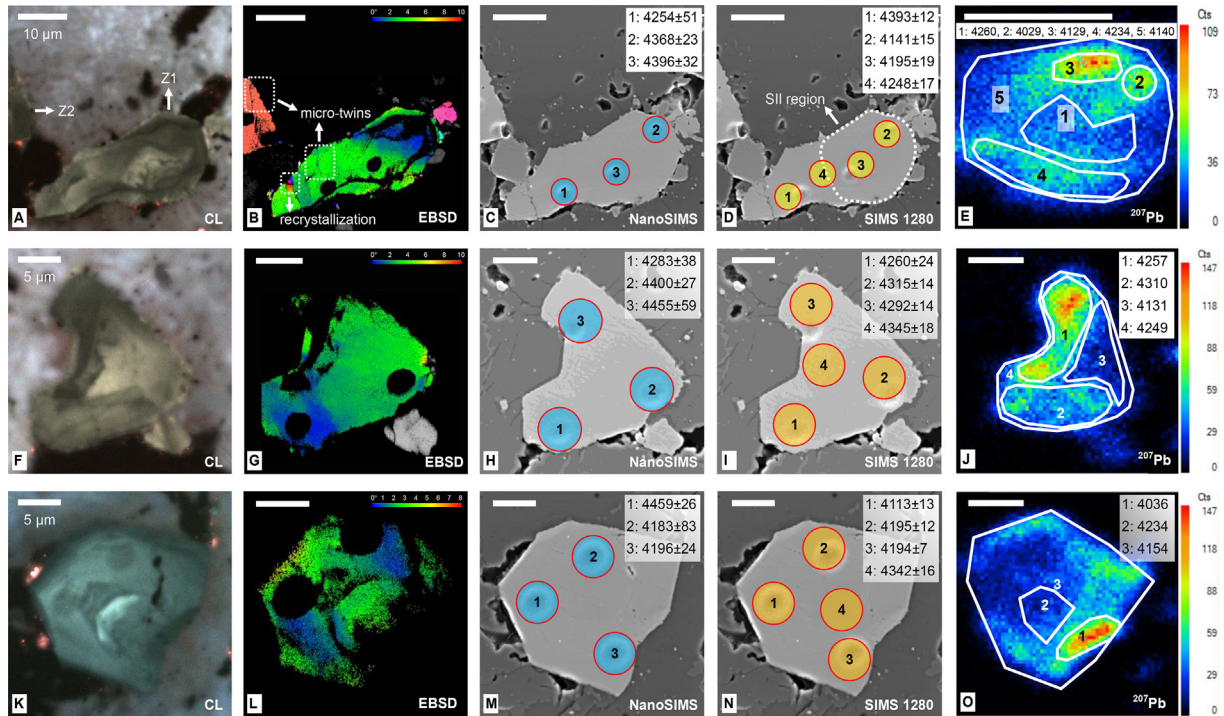| Sample	Corrected $^{207}Pb/^{206}Pb$	Err Mean (1σ %)	$^{204}Pb/^{206}Pb$	$^{207}Pb/^{206}Pb$ age (Ma)	± 1σ	NanoSIMS Spots	$^{207}Pb/^{206}Pb$ age (Ma)
Z1R-1	0.55465	0.84	0.000411	4393	12	Z1-1	4254
Z1R-2	0.46713	1.01	0.000113	4141	15	Z1-2	4368
Z1R-3	0.48455	1.26	0.000028	4195	19	Z1-3	4396
Z1R-4	0.50235	1.14	0.000063	4248	17	N/A	N/A
Z3R-1	0.50653	1.65	0.000213	4260	24	Z3-1	4283
Z3R-2	0.52569	0.97	0.000155	4315	14	Z3-2	4400
Z3R-3	0.51751	0.98	0.000128	4292	14	Z3-3	4455
Z3R-4	0.53670	1.21	0.000019	4345	18	N/A	N/A
Z5R-1	0.45864	0.88	0.000556	4113	13	Z5-1	4459
Z5R-2	0.48444	0.80	0.000048	4195	12	Z5-2	4183
Z5R-3	0.48420	0.49	0.000113	4194	7	Z5-3	4196
Z5R-4	0.53562	1.06	0.000044	4342	16	N/A	N/A

Fig. 7. CL imaging, EBSD crystallographic orientation mapping, NanoSIMS dating (in BSE), IMS 1280HR dating (in BSE), SII ^{207}Pb data for Z1 (A–E), Z3 (F–J), and Z5 (K–O) in thin section 72255,126. In panels B. G, and L, the opaque pits result from the primary-beam bombardment of NanoSIMS. The ages of ROIs 5, 4, and 3 in panels E, J, and O, respectively, correspond to the age of the entire zircon grain including other ROIs. All the listed ages are in million years (Ma). All the images above were acquired after the NanoSIMS session. The BSE images marked with NanoSIMS pits are used to compare IMS 1280HR pits, so the images are not indicative of the superficial morphology of zircons in the NanoSIMS session.

twins have been reported from other lunar zircons (e.g., Crow et al., 2015) and are the result of shock pressure >3 GPa (Jones et al., 2018). In addition, Z1 has two recrystallization subdomains (∼2 μm) on the grain boundary and planar deformation features (Fig. 7B). EBSD mapping also indicates that crystallinity is low to absent in zones spatially correlated with low CL emission, an association usually explained by locally higher actinide concentrations and metamictization. Some zircon grains (Z6, Z7, and Z8) are entirely metamict. These metamict and dark-CL subdomains have high concentrations of Pb* according to the SII (Fig. 7). In summary, the Civet Cat norite zircons demonstrate primary features like euhedral to subhedral forms and planar growth zoning with partial or complete metamictization and partly overprinted by shock microstructures.

3.5. Pb isotope mapping

Based on the CL patterns and metamict subdomains, several ROIs in the SII image of each zircon (Z1, Z3, and Z5) from section 72255,126 were selected to test whether ^{207}Pb/^{206}Pb age variations are spatially related to zoning patterns and/or microstructures. The ^{207}Pb/^{206}Pb ages for ROIs and whole grains reported in this section are based on SII. The SII-derived ages are heterogeneous within one grain, and all of them are younger than 4.35 Ga (Table 3). Z1 has four ROIs and one for the entire grain. Z1 ROI1

denotes the core (CL bright), and ROI2, ROI3, and ROI4 denote the rim and metamict sub-domains (CL dark). The core has the oldest age of 4260 Ma within Z1, while the other ROIs are slightly younger, although they have higher ^{207}Pb counts in SII (Fig. 7E). The entire Z1 grain (ROI5) has an integrated age of 4140 Ma. For Z3, the first three ROIs were selected based on the CL zoning, and ROI4 represents the entire grain (Fig. 7J). Z3 ROI3 is a CL dark and metamict sub-domain, and it has the highest counts of Pb among all four ROIs. Z3 ROI2 has a lower concentration of trace elements than ROI3 and has a slightly deformed sub-domain. The low-trace-element ROI3 has a slightly younger age (4131 Ma) than the high-trace-element ROI2 (4310 Ma) and ROI1 (4257 Ma). The Z3 whole grain has an age of 4249 Ma. Z5 has two sub-grain ROIs and one for the entire grain (Fig. 7O). The core (Z5 ROI2, CL bright) has the oldest age of 4234 Ma, and ROI1 (4035 Ma) is metamict and CL dark sub-domains with the highest ^{207}Pb counts in SII. The entire grain (ROI3) has an age of 4154 Ma. In all, the metamict (CL dark) sub-domains have higher Pb* counts, but their ages are younger than the cores. No subdomain dated by IMS 1280HR has an ancient age of >4.40 Ga indicated by the NanoSIMS spots. The SII age heterogeneity of these zircons is mainly attributed to growth zoning, and the discrepancy between SII ROI ages and SIMS spot ages confirms that the Pb* distribution of the zircons is uneven at depths (length scales) of ∼1 μm.

Table 3
SII-derived ages of Z1, Z3, and Z5 based on ROIs.

ROI	Metamict*	Corrected $^{207}Pb/^{206}Pb$	Err (%)	$^{207}Pb/^{206}Pb$ Age (Ma)	$\pm 1\sigma$
Z1 ROI1	N	0.50628	1.22	4260	36
Z1 ROI2	Y	0.43323	1.30	4029	39
Z1 ROI3	Y	0.46349	1.65	4129	49
Z1 ROI4	Y	0.49746	2.36	4234	70
Z1 ROI5	N/A	0.46689	0.45	4140	13
Z3 ROI1	Y	0.50539	1.00	4257	29
Z3 ROI2	N	0.52390	1.55	4310	46
Z3 ROI3	N	0.46421	2.79	4131	83
Z3 ROI4	N/A	0.50268	0.84	4249	25
Z5 ROI1	Y	0.43524	1.17	4036	35
Z5 ROI2	N	0.49772	2.02	4234	60
Z5 ROI3	N/A	0.47121	0.49	4154	15

* In this column, Y, N, and N/A mean yes, no, and not applicable (as for the whole grain), respectively.

4. DISCUSSION

4.1. Petrogenesis of Civet Cat norite and its zircons

4.1.1. Civet Cat norite

The Civet Cat norite is thought to have originated in the deep crust because of its mineralogy, relict cumulate texture, and lack of meteoritic component (Wolfe, 1974), and the study of its pyroxene lamellae composition analysis suggested a paleodepth of 10–70 km (Takeda et al., 1982). Based on these petrological and geochemical characteristics, the norite clast is classified as a highly pristine rock (8/9 in the pristinity index) from the deep crust (Shearer et al., 2015). However, previous studies suggested that the Civet Cat norite has been contaminated by the 72255 impact melt because it has: (1) similar REE pattern (slope) to the 72255 matrix (Blanchard et al., 1975); (2) a less abundant REE budget, slightly negative Eu anomaly, and lower Ti/Sm, Sc/Sm compared with the other samples from Boulder 1 (Blanchard et al., 1975); (3) higher REE and much less Eu in the whole-rock than the other Apollo 17 norites (Winzer et al., 1975); (4) potential addition of Rb into the pyroxene during its emplacement into the breccia (Compston et al., 1975); and (5) Pb introduced into the plagioclase-rich fraction of the clast at 3.9–4.0 Ga (Nunes and Tatsumoto, 1975).

After excavation from the deep crust, the Civet Cat norite was incorporated into the 72255 matrix during the same, or a later, impact event. The clast has a minimum crystallization age of 4.16 ± 0.05 Ga (2σ) based on the Rb-Sr system (Compston et al., 1975). Its SIMS U-Pb dating of phosphates and Ar-Ar dating provide younger ages of 3930 ± 13 Ma (Thiessen et al., 2017) and 3.99 ± 0.03 Ga (Leich et al., 1975), respectively. The consistent impact ages by Ar-Ar and Pb-Pb dating indicate that the norite was embedded into the matrix at 3.93 Ga or earlier. In summary, the norite clast formed in the deep crust before 4.16 Ga and was incorporated into the 72255 matrix at no later than 3.93 Ga. The norite clast represents a pristine lithology of the deep lunar crust, and it may include signatures constraining the differentiation of ancient lunar crust.

4.1.2. Zircon paragenesis

The microstructural and trace-element similarities of the micro-zircons observed in the Civet Cat norite lead us to interpret their paragenesis as igneous grains that co-crystallized with the norite cumulate minerals prior to modification by later shock metamorphism. The subhedral, and sometimes near euhedral, habits are unlikely to have survived if the grains were xenocrysts (see Section 3.4). Together with the petrogenesis of the Civet Cat norite, it is proposed that the zircons crystallized in a deep lunar crust (Mg-suite) and were excavated due to an impact at 3.92 Ga based on the aphanitic matrix age data. Some of the shock deformations could have also been accumulated during the final event exposing the boulder at 55 Ma (Leich et al., 1975), although there is no evidence of U-Pb isotopic disturbance at this relatively young age.

4.2. "Oldest lunar U-Pb ages

Among the 42 analytical spots, the six oldest spots (Z3-3, Z5-1, Z10-2, Z14-1, Z16, and Z18-2) define a weighted mean $^{207}Pb/^{206}Pb$ age of 4453 ± 34 Ma (2σ, MSWD = 0.056, P = 0.998; Fig. 8B) and a concordant U-Pb average age of 4460 ± 31 Ma (2σ, MWSD = 0.47, P = 0.92; Fig. 8A) on the Wetherill Concordia diagram.

The U-Pb ages above are the oldest reported for lunar zircons so far. They are significantly older than the $^{207}Pb/^{206}Pb$ age peak of the majority of lunar zircons at ~4.34 Ga (Borg et al., 2015 and references therein) and ostensibly older than the previous oldest reported zircon age at 4417 ± 6 Ma (Nemchin et al., 2009a) taken from the same boulder as our sample. Ancient lunar igneous zircons are used as a tool to constrain the differentiation of the lunar interior because it is associated with magmas that were enriched in incompatible elements and thus crystallized exclusively within the LMO residue – KREEP-rich magmas (Nemchin et al., 2009a). Therefore, our concordant U-Pb ages of magmatic zircons from the Civet Cat norite could support the extremely rapid crystallization of the LMO and be the first direct geochronological evidence that the Giant Impact occurred within the first 100 million years of the solar system.
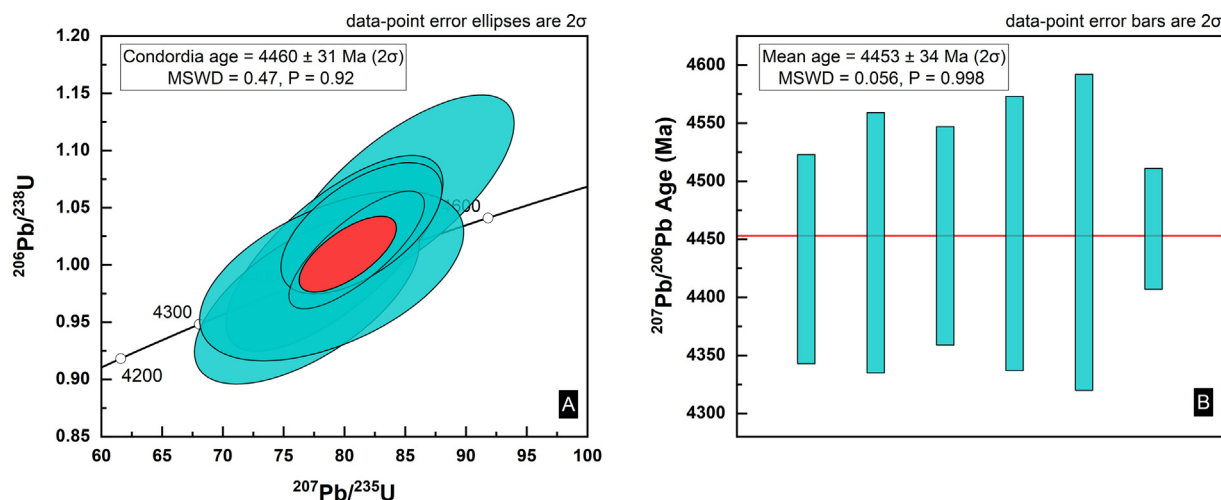
Fig. 8. NanoSIMS U-Pb ages (A) and weighted mean ^{207}Pb/^{206}Pb age (B) of the six oldest subdomains.

If the 4460 Ma U-Pb and 4453 Ma Pb-Pb ages are accurate, our results have the potential to change the way we view the early evolution of the Moon. In this case, they would place an age bracket on the timing of the Giant Impact and subsequent LMO crystallization between 4.51 Ga (Barboni et al., 2017) and 4.46 Ga. Furthermore, these U-Pb ages would be significantly older than the lunar hemisphere-wide homogenization at 4.34–4.37 Ga constrained by different radiometric systems across different lunar rock types (Borg et al., 2015 and references therein). When we take the "oldest" zircon ages into account, this later ~4.35 Ga event may have to be ascribed to secondary large-scale magmatism after the LMO crystallized. However, the accuracy of the 4.46-Ga U-Pb age should be further addressed before applying it to the current LMO models. One major concern for the "oldest" ages is that they could result from unsupported Pb* within the Civet Cat norite zircons. The enrichment of unsupported Pb* in ancient zircons may lead to spurious ^{207}Pb/^{206}Pb ages (e.g., Ge et al., 2018; 2019; Kusiak et al., 2013b; Whitehouse et al., 2014; Williams et al., 1984) and sometimes pseudo-concordant U-Pb ages (Ge et al., 2018; 2019) in ion-microprobe analyses, which ultimately result in the misinterpretation of their crystallization age. The effect of Pb* enrichment could become significant when the analytical spot size by ion microprobes is reduced to a few micrometres.

Radiogenic Pb enrichment is produced by intra-grain Pb* mobilization instead of in situ U decays, and the enrichment usually presents as nanometre-scale to micrometre-scale domains (Ge et al., 2019 and references therein) or as metal Pb (Kusiak et al., 2015; Whitehouse et al., 2017) and Pb oxides (Kusiak et al., 2019). These Pb* enrichment domains and Pb-rich phases are usually smaller than the sputtering volume of ion-microprobe primary beams. The Pb* enrichment may result in concordant yet unsupported U-Pb ages. Ge et al. (2018) reported a Jack Hills zircon grain (14041) that has a concordant U-Pb age of 4463 Ma, but this age was interpreted as a result of Pb* mobilization caused by later recrystallization and fluid

infiltration. In addition to the possible presence of Pb* enrichment, the U-Pb average age of 4461 ± 33 Ma from six spots reported here could be challenged in regard to constraining the crystallization model of the Civet Cat norite zircons due to the large uncertainty of the individual ^{206}Pb/^{238}U ages (up to 268 Ma in 2σ) (Table 1). Therefore, the "oldest" NanoSIMS U-Pb dating results of the Civet Cat norite zircons need to be carefully evaluated.

Several empirical criteria have been established to identify Pb* enrichment during ion-microprobe analyses: wide variations of within-run Pb counts, wide age variations of the same locations on repolished surfaces, and reverse discordance of oldest spots (Ge et al., 2018 and references therein). For the Civet Cat norite zircons, although the reverse discordance is absent in all spots (Fig. 5A), the standard deviations of ^{206}Pb and ^{207}Pb counts of the "oldest" grains are similar to their statistic uncertainties by a factor <2 (Fig. 9), and the variation (20–30%) of ^{206}Pb and ^{207}Pb counts in each cycle is similar to those of the Jack Hills zircon 14041 (Ge et al., 2018). More importantly, there are blocks with abnormally ancient ^{207}Pb/^{206}Pb ages (>4567 Ma) in the "oldest" zircon grains (Fig. 9). It should also be noted that the ^{207}Pb/^{206}Pb ages within one zircon grain (e.g., Z3 and Z5) can vary more than 250 Ma while their respective U-Pb ages are concordant. The wide age variations are due to either microstructural heterogeneity (different ages of growth zoning) or, more likely, Pb* mobilization caused by loss and local intracrystalline enrichment, considering the large age errors. These signatures suggest the potential presence of Pb* enrichment domains within the micro-zircons, but not the metallic Pb nanospheres that are required to significantly affect age interpretations as modelled in Ge et al. (2019).

4.3. Heterogenous distribution of intra-grain Pb*

This section presents a quantitative investigation of the occurrence of Pb* mobilization in the Civet Cat norite zircons. The potential occurence of Pb* enrichment domains in the micro-zircons can account for the large ^{207}Pb/^{206}Pb
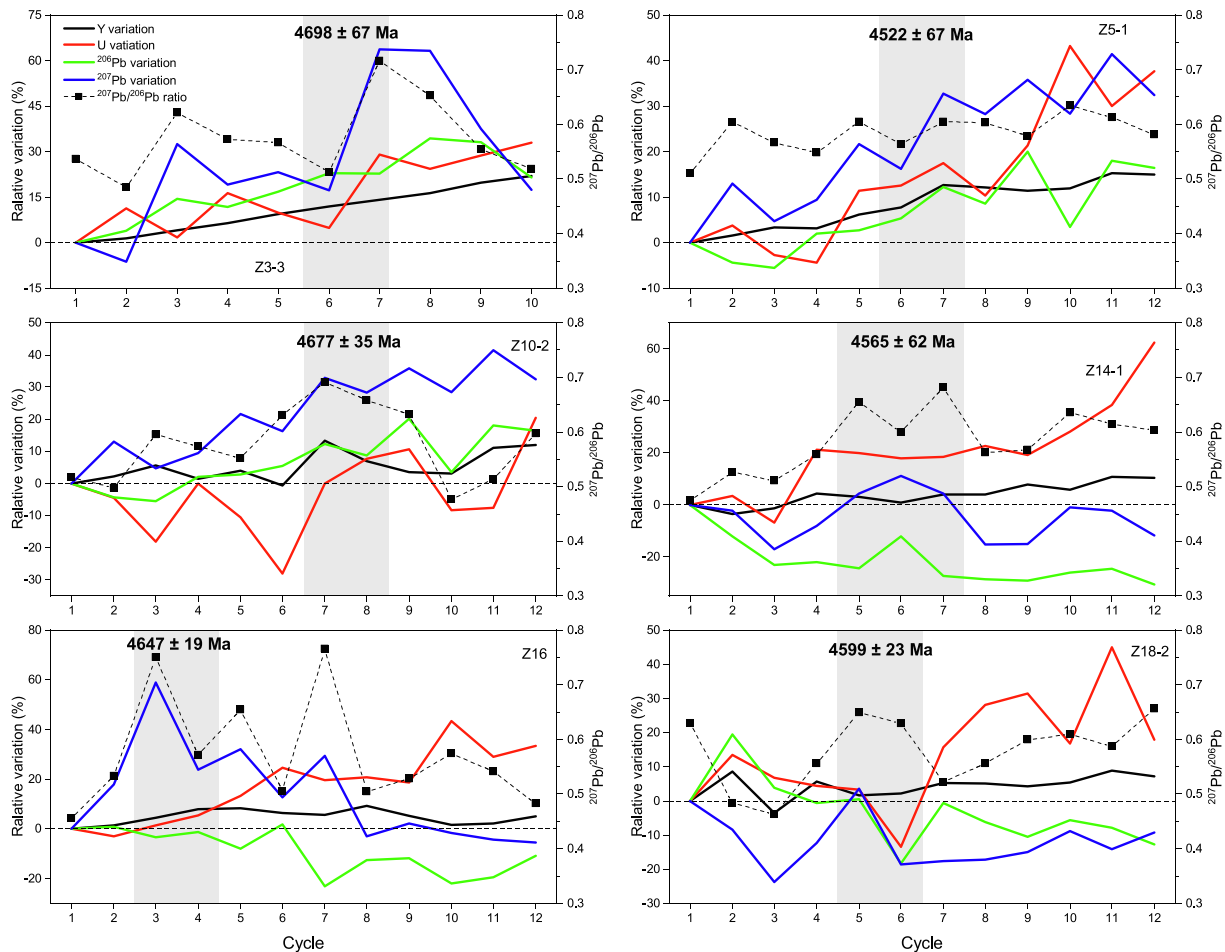
Fig. 9. In-run Pb, Y, and U variation compared with the first cycle and absolute ^{207}Pb/^{206}Pb ratios in the NanoSIMS session for the six oldest sub-domains of micro-zircons from the Civet Cat Norite thin sections 72255,123 and 72255,126. The grey areas denote the oldest block (consisting of 2–3 cycles) of each spot, and the ^{207}Pb/^{206}Pb ages are not calibrated with common Pb. The running time for each cycle of ^{207}Pb usually had ∼2 times more than that of ^{206}Pb. The original data are listed in Appendix 7.

age uncertainties (i.e., wide within-run variations of ^{207}Pb/^{206}Pb ratios) in both NanoSIMS (26–200 Ma at 2σ levels) and IMS 1280HR (14–48 Ma) sessions. The cycles with large analytical uncertainties often have anomalously higher ^{207}Pb/^{206}Pb ratios, hence extremely ancient ages for some cycles (Fig. 9). One possibility is that the NanoSIMS recorded a false signature due to the discharge of static electricity. In this case, all detectors should have recorded the same false counts. However, the background (203.5 amu) and ^{204}Pb (204 amu) showed no intensity measurements induced by the discharge of static electricity. Alternatively, because ^{206}Pb and ^{207}Pb were counted separately during the NanoSIMS sessions, some clusters of Pb were sputtered out within 10 s, causing a count spike and variation in ^{207}Pb/^{206}Pb ratios. This effect can be remarkable for the low counting rate of ^{207}Pb when the target area is small (3 × 3 μm), but it was not observed in the Nano-SIMS U-Pb dating of the zircons in lunar meteorite Sayh al Uhaymir 169 (Hu et al., 2016). In the later IMS 1280HR session, cycle 1 of Z3R-4, again, has a prominent ^{207}Pb count spike and an unsupported ^{207}Pb/^{206}Pb age of

4605 Ma (common Pb corrected). One explanation would be that the SIMS spots with ^{207}Pb/^{206}Pb ratio spikes covered Pb* enrichment domains. The obvious but sporadic ^{207}Pb/^{206}Pb ratio spikes during the analyses imply that the Pb* enrichment domains (if present) of Civet Cat norite zircons are much smaller than the primary-beam sputtering volume, and the ion microprobe beams bombarded both supported and unsupported Pb* in a single measurement.

The dating results for three consecutive surfaces by NanoSIMS, SII, and IMS 1280HR indicate that the Pb* distribution of the 72255,126 zircons is heterogeneous among different subdomains and polishing or sputtering surfaces. The heterogeneity of Pb* distribution is further supported by the distinct ages (difference of >100 Ma) within one single grain such as Z3, Z5, Z7, Z12, and Z18 (Table 1), especially the inconsistent dates (4183 Ma, 4196 Ma, and 4459 Ma) of the growth zoning rim of Z3. Moreover, the Pb* distribution seems to vary with polishing or sputtering depth. Except for analytical spots Z5-2 and Z5-3 (superposing Z5R-2 and Z5R-3, respectively), all the other spots by IMS 1280HR cannot reproduce the

NanoSIMS results (Table 1 and Fig. 7). In an extreme situation, the uppermost surface dated by NanoSIMS has an age of 4459 ± 26 Ma (Z5-1), but on the freshly sputtered surface after SII, this spot is more than 300 Ma younger (Z5R-1 = 4113 ± 13 Ma) dated by IMS 1280HR. The large age discrepancy between different polishing zircon surfaces is one of the signs for intra-grain Pb* mobilization (Ge et al., 2018) in the Civet Cat norite zircons.

Due to these complicated Pb* distribution patterns and the lack of high-precision U-Pb ages to resolve the lower and upper intercepts on the Wetherill Concordia diagram (Fig. 5A), it is difficult to unequivocally interpret the crystallization age and later metamorphism age from the Concordia diagram for the Civet Cat norite zircons. Nonetheless, the combined SII and SIMS dating can still provide constraints on the crystallization age. According to the SII and ROIs dating, the whole grains of Z1, Z3, and Z5 have ages of 4140 Ma, 4240 Ma, and 4154 Ma, respectively (Fig. 7 and Table 3). Also, it seems that some subdomains in Z5 are devoid of Pb* mobilization. The growth zoning rim has reproducible ages at Z5-2 (Z5R-2) and Z5-3 (Z5R-3), and these four ages define a weighted mean age of 4194 ± 6 Ma (2σ, MSWD = 0.17, P = 0.92). This age is close to the whole-grain age of Z5 at 4154 Ma. The 4.19 Ga age is also consistent (within error) with the Rb-Sr isochron age of 4.16 ± 0.05 Ga (Compston et al., 1975). The age of 4194 ± 6 Ma represents the minimum crystallization for the rim and be the youngest age estimate for the Civet Cat norite zircons if they are cogenetic (see Section 4.1.2). In all, the Civet Cat norite zircons are interpreted here to have crystallized ≥ 4.19 Ga and have experienced one major shock-metamorphic event at 3.92 Ga (see Section 4.1.1).

4.4. Elusive crystallization age of the Civet Cat norite zircons

In Ge et al. (2018)'s model of Pb* mobilization, they predict that inaccurate ancient U-Pb ages and mobilization hinge on the zircon grain experiencing a history of fluid alteration (with or without metamictization). Unsupported Pb* is locally clustered to produce reverse discordance, or, in addition, that the Pb-clustered grain undergoes a much later Pb loss event to (fortuitously) return the U-Pb composition to a false position on the Concordia curve. However, their model did not consider the possibility that domains of normal Pb loss, beyond the Pb-depletion halos, could form at the same time as Pb clusters. A recent study has documented this scenario in the shock metamorphosed zircons from the ultra-high temperature (UHT) zone of the central uplift at the 2.020 Ga Vredefort impact structure of South Africa (Arcuri et al., 2020). In their work, atom probe results revealed nanodomains of Pb clustering, interspersed at micrometre scale with nanodomains of 100% Pb loss in the V09-237-G4 grain. This kind of accelerated Pb loss and clustering requires extreme diffusion rates and was interpreted to have been caused by impact shock deformation along with intrusion of fine networks of impact melt veins. The end results of the Vredefort grains have very small spatial variations in discordance and $^{207}Pb/^{206}Pb$ ages varying by several hundred million years (Moser et al.,

2009), which are strikingly similar to those of the Civet Cat norite (Fig. 5). The Vredefort grain is from the central uplift that was crystalline in mid-crust at the time of impact but is now at surface. Considering the similar geological settings and geochronologic patterns, the Vredefort grain is analogous to the Civet Cat norite grains. Their geologic history contrasts with the history of typical terrestrial tectonic environments (Ge et al., 2018; 2019; Kusiak et al., 2013a; 2013b; 2015; Piazolo et al., 2016; Reddy et al., 2016). So, in light of the new results by Arcuri et al. (2020), it remains possible that the oldest zircon dates reflect the crystallization age of the norite and that the U-Pb systematics reflect variable mixtures of submicrometre domains of Pb retention and Pb loss, and varying normal discordance, intersected by the different polishing surfaces.

It should be noted that the Civet Cat norite zircons have no reversely discordant ancient spots that were usually reported in other terrestrial zircons with Pb* enrichment (Ge et al., 2018; 2019; Kusiak et al., 2013a; 2013b; Whitehouse et al., 2014; Williams et al., 1984). On the Tera-Wasserburg diagrams (Appendices 5A and 5B), there are two possible arrays of ellipses found: the first one with shallow-angle ellipses as for Z8 (Appendix 5H) and Z12 (Appendix 5L) and another one with ellipses parallel to the Concordia curve as shown by the collective spots (similar to the Concordia diagram of the V09-237-G4 grain from Arcuri et al., 2020). The shallow-angle age arrays could possibly be induced by ancient Pb* enrichment domains of Z8 and Z12 at a much later event (Ge et al., 2018). The Pb* enrichment domains or Pb-rich phases, if present, could be high enough in concentrations to shift a SIMS analysis to the left or dramatically upwards by hundreds of Ma along the concordia curve on the Tera-Wasserburg diagram (Ge et al., 2018; Kusiak et al., 2015). Due to the lack of SII of Z8 and Z12, we are not able to assess if these two grains have such Pb* enrichment domains or Pb-rich phases. Several other observations, however, support that Pb* enrichment domains or Pb-rich phases do not account for the shallow-angle ellipse array of Z8 and Z12. First, the Pb* enrichment domains with reverse discordance in the Jack Hills zircon (Ge et al., 2018) have high U concentrations, while the U contents of Z8 (81–137 ppm) and Z12 (23–57 ppm) are at a low or intermediate level compared with those of other Civet Cat norite zircons. In addition, Z8 and Z12 do not show any Pb loss event on the Tera-Wasserburg diagram as is shown in the Jack Hills zircon (Ge et al., 2018). As for the six oldest spots of the high-angle ellipse array, they are highly concordant and consistent (MWSD = 1.15) on the Tera-Wasserburg diagram (Appendix 5P). The only exception is Z3-3 with an intermediate U content (95 ppm) and a Pb hotspot (Fig. 7J), while Z5-1, Z10-2, Z14-1, Z16, and Z18-2 have low U contents (≤52 ppm) (Appendix 6). The concordant U-Pb and Pb-Pb ages with low U contents are not consistent with those documented by Ge et al. (2018) and Kusiak et al. (2015). Second, in both situations of Ge et al. (2018) and Kusiak et al. (2015), Pb* enrichment domains and Pb-rich phases formed during a period of metamictization followed by intense heating. In the Civet Cat norite zircons, we did not find any metamor-

phic rims or other signs of widespread high-temperature overprint (see Section 3.4). Based on these observations, for the Civet Cat norite zircons, we prefer the Pb* distribution mechanism proposed by Arcuri et al. 2020. It is plausible that the 4.46-Ga age for the Civet Cat zircons is valid, and the heterogeneity of Pb* distribution causes the SIMS signal variations limiting the precision of their age determination. Alternatively, the absence of reverse discordance could be attributed to the low resolution of our NanoSIMS U-Pb measurements with uncertainties of >3%, which can result in U-Pb age errors of 120–220 Ma (2σ) for the >4 Ga zircons. In this case, the Pb* distribution mechanism proposed by Ge et al. (2018) is preferable for the Civet Cat norite zircons, and the old concordant U-Pb age would be biased. In conclusion, due to the lack of high-resolution mapping of the Pb* distribution patterns at this time, we cannot draw a firm conclusion about the crystallization age for the Civet Cat norite zircons.

4.5. Pinpointing the mechanism for Pb* mobilization

Regardless of the morphology of the Pb* distribution, the combined SII and SIMS spot analyses demonstrate that Pb* was mobilized within the Civet Cat norite zircons after their primary crystallization. Pinpointing the mechanism triggering the Pb* mobilization will help us understand the behaviour of zircon U-Pb isotope systematics, especially in the lunar settings. One detrital zircon grain in Apollo aphanitic impact melt breccia 73235 has been reported to have nanoscale Pb* clusters (Blum et al., 2019), which were thought to have formed during an impact event. Due to the rarity of such Pb* clusters found in extraterrestrial rocks and the lack of comprehensive investigations of the mechanism for Pb* mobilization in extraterrestrial samples, the previous studies of Pb* mobilization in terrestrial zircons are used as a reference to discuss the possible mechanisms for the lunar scenario.

For terrestrial zircons, Ge et al. (2018) concluded that Pb* mobilization is usually related to radiation damage, plastic deformation, and recrystallization. Regarding radiation damage, nanometre-scale α-recoil damage in zircon lattices facilitates the migration of Pb and other incompatible elements, and this process will be accelerated by later reheating events (Valley et al., 2014) or later UHT metamorphism (Kusiak et al., 2015). Plastic deformation-related dislocation of zircon lattices also facilitates the migration of trace elements (Kovaleva et al., 2017; MacDonald et al., 2013; Piazolo et al., 2016; Reddy et al., 2006, 2016) and hence disturb the U-Pb isotope system (Kovaleva et al., 2017). Other than these two mechanisms, Pb* can migrate at recrystallization fronts, and this process can be enhanced by fluid infiltration during metamorphic events (Ge et al., 2018, 2019). Among the Civet Cat norite zircons, except for the small recrystallization subdomains on the edge of Z1 and Z2, no other intra-grain recrystallization features were found. Moreover, no signature of fluid infiltration has been detected in the Civet Cat metaplutonic norite, and such metamorphism is unlikely to have occurred in this lunar norite, considering the Moon is generally depleted of volatiles and fluids (Boyce et al., 2014).

Hence, the mechanism of Pb* mobilization at recrystallization fronts enhanced by fluid filtration cannot fit in the situation of the Civet Cat norite. Instead, radiation damage and plastic deformation are the probable mechanisms that induced the heterogeneity of Pb* distribution found in the Civet Cat norite zircons.

The radioactive decay of U and Th can cause damage to regional lattices, amorphous sub-domains or complete loss of crystallinity (metamict) in zircon (Nasdala et al., 2001). The zircon grains in the Civet Cat norite have lost partial (most grains) or major crystallinity (e.g., Z6, Z7, and Z8) due to radiation damage according to the EBSD analyses. To quantitatively evaluate the influence of radiation damage on the zircon crystallinity, the α-decay dose of each zircon dating spot is calculated using the equation from Murakami et al. (1991).

$$D = 8 \times N_{238}\left(e^{\lambda_{238}t} - 1\right) + 7 \times N_{235}\left(e^{\lambda_{235}t} - 1\right) + 6 \\ \times N_{232}\left(e^{\lambda_{232}t} - 1\right)$$

D, N, λ, and t represent α-decay dose (events/mg), present numbers of ^{238}U, ^{235}U, and ^{232}Th (atoms/mg), decay constants (y^{-1}), and age of zircon (y), respectively. The modern $^{238}U/^{235}U$ ratio is assumed to be 137.79 for lunar rocks (Andersen et al., 2017). The results are listed in Table 1. The α-decay dose since 4194 Ma is $1.1–6.1 \times 10^{15}$ events/mg with a mean value of $2.2 \pm 1.3 \times 10^{15}$ events/mg, and the dose since 3930 Ma is $1.0–5.3 \times 10^{15}$ events/mg with a mean value of $2.1 \pm 1.1 \times 10^{15}$ events/mg. The actual α-decay dose for these zircons could be even higher because the youngest crystallization estimate was used for the dose calculation. The accumulated α-decay dose since 4194 Ma is consistent with the value of 2.2×10^{15} events/mg where zircon becomes metamict (Kusiak et al., 2015), so the α-decay since 4194 Ma accounts for the partial or complete metamictization of the Civet Cat norite zircons.

From the literature discussing radiation damage-related Pb* mobilization, the crystal damage caused by radioactive decays is a precondition for Pb* to migrate. More importantly, later reheating or metamorphic events are a critical condition that permits Pb* to form mineral phases or enrichment domains (Kusiak et al., 2015; Peterman et al., 2016; Valley et al., 2014; Whitehouse et al., 2014). Hence, during the interval of primary crystallization and later reheating (or metamorphism), the α-decay dose must reach the first percolation (become metamict) to produce zircon lattice defects. The Civet Cat norite zircons formed at >4.19 Ga and experienced major shock metamorphism at 3.93 Ga (see Sections 4.1 and 4.3). The accumulated dose between 4.19 Ga (formation) and 3.93 Ga (metamorphism) is $0.1–0.7 \times 10^{15}$ events/mg, which is significantly lower than the first percolation value of 2.2×10^{15} events/mg (Kusiak et al., 2015). Assuming that the Civet Cat zircons formed as early as the lunar global magmatism at 4.34 Ga (Borg et al., 2015), the accumulated α-decay dose between 4.34 Ga and 3.93 Ga would be $0.2–1.3 \times 10^{15}$ events/mg, which is still below the first percolation. Regardless of their crystallization age, the Civet Cat norite zircons were unlikely subjected to metamictization during the interval of primary crystallization and shock metamorphism. Therefore,

by the time of the 3.93-Ga shock metamorphism, the Civet Cat norite zircons had not developed enough radiation damage to allow for Pb* mobilization. In addition to the inadequate α-decay dose, of the six "oldest" spots, five spots (excluding Z3-3) are not on the metamict sub-domains. The analytical spots of metamict zircons Z6, Z7, and Z8 did not show extremely ancient ages. As such, the Pb* mobilization in the Civet Cat norite zircons is not directly related to radiation damage.

Deformational alterations in zircon lattices can enhance the diffusion and mobilization of trace elements (Kovaleva et al., 2017; MacDonald et al., 2013; Moser et al., 2009; Piazolo et al., 2016; Reddy et al., 2006, 2016). Kovaleva et al. (2017) concluded that trace elements can diffuse along dislocation arrays (Piazolo et al., 2016) and/or migrate from pristine lattices to defective lattices (MacDonald et al., 2013; Timms et al., 2011). The plastic deformation induced by shock metamorphism is a prevalent micro-structural feature found throughout the Civet Cat norite zircons. Each grain has at least 3–7° cumulative misorientation, and some can reach up to 10° (Z1 and Z10) and 20° (Z9). Grains Z1 and Z2 have micro-twins, and Z1 has additional planar deformation. For the "oldest" spots, we did see that Z5-1, Z10-2, and Z14-2 are located on either a crack or a plastically deformed subdomain. The deformation information of Z3-3 is concealed by its metamictization, and spots Z16 and Z18-2 were not mapped by EBSD. Based on the currently available data, the lattice defects induced by shock-related plastic deformation are the preferable mechanism that is responsible for the Pb* mobilization found in the Civet Cat norite zircons. In the mechanism of Pb* mobilization proposed by Piazolo et al. (2016), Y usually co-clusters with Pb* in the dislocations, and therefore, Y count variations in the NanoSIMS session may be an indicator of Pb* clusters. In the case of the Civet Cat norite zircons, all the spots that have an ancient age >4400 Ma (with at least one block of spiked $^{207}Pb/^{206}Pb$ ratios) do not show simultaneously spiked Y counts with $^{207}Pb/^{206}Pb$ ratios (Fig. 9 and Appendix 7). Based on this observation, the migration of Pb* and Y along dislocation arrays seems unlikely in the Civet Cat norite zircons. Due to the absence of high-resolution imaging of trace-element distribution, it is difficult to assess if the Pb* mobilization is correlated to other trace elements at a finer scale. Future studies of the Civet Cat norite zircons should focus on using high-resolution isotope imaging by NanoSIMS or atom probe tomography to investigate the distribution patterns of Pb* and other trace elements at a sub-micrometre or nanometre scale.

5. SUMMARY

This work presents a detailed petrographic study, microstructural analysis, SIMS U-Pb dating and SII analysis of micro-zircons found in the Apollo 72255 Civet Cat norite. We interpret the Civet Cat norite zircons to be igneous as they have a similar habit, internal zoning, and trace element geochemistry. Additionally, these zircons exhibit shock-metamorphic microstructures including crystallographic misorientation, micro-twins, and planar deformation features.

The U-Pb NanoSIMS data show that the six oldest spots define a weighted mean $^{207}Pb/^{206}Pb$ age of 4453 ± 34 Ma and a concordant U-Pb average age of 4460 ± 31 Ma. The NanoSIMS $^{207}Pb/^{206}Pb$ ages within one zircon grain (e.g., Z3 and Z5) can vary by more than 250 Ma. More importantly, the IMS 1280HR ages of the same spots analyzed in the NanoSIMS session but from repolished surfaces are significantly younger. Some analytical cycles in both NanoSIMS and IMS 1280HR sessions have spikes of $^{207}Pb/^{206}Pb$ ratios. The SII analysis confirms that the distribution of Pb* and $^{207}Pb/^{206}Pb$ ages are heterogeneous within a single zircon grain and zoning band.

We propose that one mechanism that may have facilitated the Pb* mobilization is most likely associated with lattice defects induced by shock-related plastic deformation as all zircons in the Civet Cat norite have at least 3–7° of cumulative misorientation. Another possible mechanism, the structural damage caused by radioactive decay, is precluded because the accumulated α-decay dose between the (tentative) crystallization and metamorphism of the zircons was not sufficient to allow for radiation damage. This study highlights that slightly shock-deformed zircons are subject to Pb* mobilization.

Radiogenic Pb clustering should result in reverse discordance (mixing of Pb* nanoclusters and in situ Pb from U decay) (Ge et al., 2018) or normal discordance (mixing of Pb retention and Pb loss) (Arcuri et al., 2020). We observe no reverse discordance of the ancient spots (as the evidence for pseudo-concordance) but an array of all error ellipses spread along, and at or near, Concordia on the Wetherill diagram and the Tera-Wasserburg diagram, and find that the six oldest domains have consistent $^{207}Pb/^{206}Pb$ ages within errors. Therefore, it remains possible that the Pb-retention domains in the norite zircons are mixed with Pb-loss domains. If this is the case, the 4.46 ± 0.03 Ga U-Pb average age of the zircons would possibly be the oldest mineral record for the Moon providing a minimum age for its formation. Alternatively, the relatively large errors of the NanoSIMS U-Pb ages may conceal reverse discordance. In this case, mixing of mobilized ancient Pb* and Pb* produced by in situ U decay would bias an apparently concordant U-Pb analysis.

Declaration of Competing Interest

The authors declare that they have no known competing financial interests or personal relationships that could have appeared to influence the work reported in this paper.

APPENDIX A. SUPPLEMENTARY MATERIAL

Supplementary data to this article can be found online at https://doi.org/10.1016/j.gca.2021.03.012.

REFERENCES

Andersen M. B., Stirling C. H. and Weyer S. (2017) Uranium isotope fractionation. *Rev. Mineral. Geochem.* **82**, 799–850.

Arcuri G. A., Moser D. E., Reinhard D. A., Langelier B. and Larson D. J. (2020) Impact-triggered nanoscale Pb clustering and Pb loss domains in Archean zircon. *Contrib. Mineral. Petr.* **175**, 59.

Barboni M., Boehnke P., Keller B., Kohl I. E., Schoene B., Young E. D. and McKeegan K. D. (2017) Early formation of the Moon 4.51 billion years ago. *Sci. Adv.* **3**, e1602365.

Blanchard D. P., Haskin L. A., Jacobs J. W., Brannon J. C. and Korotev R. L. (1975) Major and trace element chemistry of Boulder 1 at Station 2, Apollo 17. *Earth Moon Planets* **14**, 359–371.

Blum T. B., Reinhard D. A., Coble M. A., Spicuzza M. J., Chen Y., Cavosie A. J., Nasdala L., Chanmuang C., Prosa T. J., Larson D. J. and Valley J. W. (2019) A nanoscale record of impact-induced Pb mobility in lunar zircon. *Microsc. Microanal.* **25**, 2448–2449.

Borg L. E., Gaffney A. M. and Shearer C. K. (2015) A review of lunar chronology revealing a preponderance of 4.34–4.37 Ga ages. *Meteorit. Planet. Sci.* **50**, 715–732.

Boyce J. W., Tomlinson S. M., McCubbin F. M., Greenwood J. P. and Treiman A. H. (2014) The lunar apatite paradox. *Science* **344**, 400–402.

Černok A., White L. F., Darling J., Dunlop J. and Anand M. (2019) Shock-induced microtextures in lunar apatite and merrillite. *Meteorit. Planet. Sci.* **54**, 1262–1282.

Cherniak D. J. (2010) Diffusion in accessory minerals: Zircon, titanite, apatite, monazite and xenotime. *Rev. Mineral. Geochem.* **72**, 827–869.

Compston W., Foster J. J. and Gray C. M. (1975) Rb-Sr ages of clasts from within Boulder 1, Station 2, Apollo 17. *The Moon* **14**, 445–462.

Connelly J. N. and Bizzarro M. (2016) Lead isotope evidence for a young formation age of the Earth-Moon system. *Earth Planet. Sci. Lett.* **452**, 36–43.

Corfu F. (2013) A century of U-Pb geochronology: The long quest towards concordance. *Bulletin* **125**, 33–47.

Corfu F., Hanchar J. M., Hoskin P. W. and Kinny P. (2003) Atlas of zircon textures. *Rev. Mineral. Geochem.* **53**, 469–500.

Crow C. A., McKeegan K. D. and Moser D. E. (2016) Coordinated U-Pb geochronology, trace element, Ti-in-zircon thermometry and microstructural analysis of Apollo zircons. *Geochim. Cosmochim. Acta* **202**, 264–284.

Dalrymple G. B. and Ryder G. (1996) Argon-40/argon-39 age spectra of Apollo 17 highlands breccia samples by laser step heating and the age of the Serenitatis basin. *J. Geophys. Res. Planets* **101**, 26069–26084.

Ge R., Wilde S. A., Nemchin A. A., Whitehouse M. J., Bellucci J. J. and Erickson T. M. (2019) Mechanisms and consequences of intra-crystalline enrichment of ancient radiogenic Pb in detrital Hadean zircons from the Jack Hills, Western Australia. *Earth Planet. Sci. Lett.* **517**, 38–49.

Ge R., Wilde S. A., Nemchin A. A., Whitehouse M. J., Bellucci J. J., Erickson T. M., Frew A. and Thern E. R. (2018) A 4463 Ma apparent zircon age from the Jack Hills (Western Australia) resulting from ancient Pb mobilization. *Geology* **46**, 303–306.

Grange M., Nemchin A., Pidgeon R., Timms N., Muhling J. and Kennedy A. (2009) Thermal history recorded by the Apollo 17 impact melt breccia 73217. *Geochim. Cosmochim. Acta* **73**, 3093–3107.

Grange M., Nemchin A., Timms N., Pidgeon R. and Meyer C. (2011) Complex magmatic and impact history prior to 4.1 Ga recorded in zircon from Apollo 17 South Massif aphanitic breccia 73235. *Geochim. Cosmochim. Acta* **75**, 2213–2232.

Hao J.-L., Yang W., Luo Y., Hu S., Yin Q.-Z. and Lin Y.-T. (2016) NanoSIMS measurements of trace elements at the micron scale interface between zircon and silicate glass. *J. Anal. At. Spectrom.* **31**, 2399–2409.

Hopkins M. and Mojzsis S. (2015) A protracted timeline for lunar bombardment from mineral chemistry, Ti thermometry and U-Pb geochronology of Apollo 14 melt breccia zircons. *Contrib. Mineral. Petr.* **169**, 1–18.

Hu S., Lin Y., Yang W., Wang W.-R., Zhang J., Hao J. and Xing W. (2016) NanoSIMS imaging method of zircon U-Pb dating. *Sci. China Earth Sci.* **59**, 2155–2164.

Hurwitz D. and Kring D. A. (2016) Identifying the geologic context of Apollo 17 impact melt breccias. *Earth Planet. Sci. Lett.* **436**, 64–70.

James O. B. (1983) Mineralogy and petrology of the pristine rocks. *Pristine Highlands Rocks Early History Moon*, 44.

Jones G., Moser D. E. and Shieh S. R. (2018) A numerical model for twin nucleation in shocked zircon and comparison with natural samples. *Geophys. Res. Lett.* **45**, 10,298–10,304.

Kovaleva E., Klötzli U., Habler G., Huet B., Guan Y. and Rhede D. (2017) The effect of crystal-plastic deformation on isotope and trace element distribution in zircon: Combined BSE, CL, EBSD, FEG-EMPA and NanoSIMS study. *Chem. Geol.* **450**, 183–198.

Kusiak M. A., Dunkley D. J., Wirth R., Whitehouse M. J., Wilde S. A. and Marquardt K. (2015) Metallic lead nanospheres discovered in ancient zircons. *Proc. Natl. Acad. Sci. USA* **112**, 4958–4963.

Kusiak M. A., Kovaleva E., Wirth R., Klötzli U., Dunkley D. J., Yi K. and Lee S. (2019) Lead oxide nanospheres in seismically deformed zircon grains. *Geochim. Cosmochim. Acta* **262**, 20–30.

Kusiak M. A., Whitehouse M. J., Wilde S. A., Dunkley D. J., Menneken M., Nemchin A. A. and Clark C. (2013a) Changes in zircon chemistry during Archean UHT metamorphism in the Napier Complex, Antarctica. *Am. J. Sci.* **313**, 933–967.

Kusiak M. A., Whitehouse M. J., Wilde S. A., Nemchin A. A. and Clark C. (2013b) Mobilization of radiogenic Pb in zircon revealed by ion imaging: Implications for early Earth geochronology. *Geology* **41**, 291–294.

Lee J. K. W., Williams I. S. and Ellis D. J. (1997) Pb, U and Th diffusion in natural zircon. *Nature* **390**, 159–162.

Leich D. A., Kahl S. B., Kirschbaum A. R., Niemeyer S. and Phinney D. (1975) Rare gas constraints on the history of Boulder 1, Station 2, Apollo 17. *The Moon* **14**, 407–444.

Li X. H., Liu Y., Li Q. L., Guo C. H. and Chamberlain K. R. (2009) Precise determination of Phanerozoic zircon Pb/Pb age by multicollector SIMS without external standardization. *Geochem. Geophy. Geosy.*, 10.

Lin Y., Shen W., Liu Y., Xu L., Hofmann B. A., Mao Q., Tang G. Q., Wu F. and Li X. H. (2012) Very high-K KREEP-rich clasts in the impact melt breccia of the lunar meteorite SaU 169: New constraints on the last residue of the Lunar Magma Ocean. *Geochim. Cosmochim. Acta* **85**, 19–40.

Liu D., Jolliff B. L., Zeigler R. A., Korotev R. L., Wan Y., Xie H., Zhang Y., Dong C. and Wang W. (2012) Comparative zircon U-Pb geochronology of impact melt breccias from Apollo 12 and lunar meteorite SaU 169, and implications for the age of the Imbrium impact. *Earth Planet. Sci. Lett.* **319-320**, 277–286.

Liu Y., Li X.-H., Li Q.-L., Tang G.-Q. and Yin Q.-Z. (2011) Precise U-Pb zircon dating at a scale of <5 micron by the CAMECA 1280 SIMS using a Gaussian illumination probe. *J. Anal. At. Spectrom.* **26**, 845–851.

Liu Y., Li Q. L., Ling X. X., Tang G. Q., Li J. and Li X. H. (2020a) Impact and correction of analytical positioning on accuracy of zircon U-Pb dating by SIMS. *Front. Chem.* **8**, 1101.

Liu Y. u., Li X.-H., Li Q.-L. and Tang G.-Q. (2020b) Break-through of 2- to 3-μm scale U-Pb zircon dating using Cameca IMS-1280HR SIMS. *Surf. Interface. Anal.* **52**, 214–223.

MacDonald J. M., Wheeler J., Harley S. L., Mariani E., Good-enough K. M., Crowley Q. and Tatham D. (2013) Lattice distortion in a zircon population and its effects on trace element mobility and U-Th-Pb isotope systematics: examples from the Lewisian Gneiss Complex, northwest Scotland. *Contrib. Mineral. Petr.* **166**, 21–41.

McDonough W. F. and Sun S.-S. (1995) The composition of the Earth. *Chem. Geol.* **120**, 223–253.

Meyer C., Williams I. S. and Compston W. (1996) Uranium-lead ages for lunar zircons: Evidence for a prolonged period of granophyre formation from 4.32 to 3.88 Ga. *Meteorit. Planet. Sci.* **31**, 370–387.

Mezger K. and Krogstad E. (1997) Interpretation of discordant U-Pb zircon ages: An evaluation. *J. Metamorph. Geol.* **15**, 127–140.

Morbidelli A., Marchi S., Bottke W. F. and Kring D. A. (2012) A sawtooth-like timeline for the first billion years of lunar bombardment. *Earth Planet. Sci. Lett.* **355**, 144–151.

Moser D., Cupelli C., Barker I., Flowers R., Bowman J., Wooden J. and Hart J. (2011) New zircon shock phenomena and their use for dating and reconstruction of large impact structures revealed by electron nanobeam (EBSD, CL, EDS) and isotopic U-Pb and (U-Th)/He analysis of the Vredefort dome. *Can. J. Earth Sci.* **48**, 117–139.

Moser D., Davis W., Reddy S., Flemming R. and Hart R. (2009) Zircon U-Pb strain chronometry reveals deep impact-triggered flow. *Earth Planet. Sci. Lett.* **277**, 73–79.

Murakami T., Chakoumakos B. C., Ewing R. C., Lumpkin G. R. and Weber W. J. (1991) Alpha-decay event damage in zircon. *Am. Mineral.* **76**, 1510–1532.

Nasdala L., Hofmeister W., Norberg N., Martinson J. M., Corfu F., Dörr W., Kamo S. L., Kennedy A. K., Kronz A. and Reiners P. W. (2008) Zircon M257 - a homogeneous natural reference material for the ion microprobe U-Pb analysis of zircon. *Geostand. Geoanal. Res.* **32**, 247–265.

Nasdala L., Wenzel M., Vavra G., Irmer G., Wenzel T. and Kober B. (2001) Metamictisation of natural zircon: accumulation versus thermal annealing of radioactivity-induced damage. *Contrib. Mineral. Petr.* **141**, 125–144.

Nemchin A. A., Pidgeon R. T., Healy D., Grange M. L., Whitehouse M. J. and Vaughan J. (2009a) The comparative behavior of apatite-zircon U-Pb systems in Apollo 14 breccias: Implications for the thermal history of the Fra Mauro Formation. *Meteorit. Planet. Sci.* **44**, 1717–1734.

Nemchin A. A., Pidgeon R. T., Whitehouse M. J., Vaughan J. P. and Meyer C. (2008) SIMS U-Pb study of zircon from Apollo 14 and 17 breccias: implications for the evolution of lunar KREEP. *Geochim. Cosmochim. Acta* **72**, 668–689.

Nemchin A., Timms N., Pidgeon R., Geisler T., Reddy S. and Meyer C. (2009b) Timing of crystallization of the lunar magma ocean constrained by the oldest zircon. *Nat. Geosci.* **2**, 133–136.

Nunes P. D. and Tatsumoto M. (1975) U-Th-Pb systematics of selected samples from Apollo 17, Boulder 1, Station 2. *The Moon* **14**, 463–471.

Paces J. B. and Miller J. D. (1993) Precise U-Pb ages of Duluth complex and related mafic intrusions, northeastern Minnesota: Geochronological insights to physical, petrogenetic, paleomagnetic, and tectonomagmatic processes associated with the 1.1 Ga midcontinent rift system. *J. Geophys. Res. Solid Earth* **98**, 13997–14013.

Peterman E. M., Reddy S. M., Saxey D. W., Snoeyenbos D. R., Rickard W. D. A., Fougerouse D. and Kylander-Clark A. R. C. (2016) Nanogeochronology of discordant zircon measured by atom probe microscopy of Pb-enriched dislocation loops. *Sci. Adv.* **2**, e1601318.

Piazolo S., La Fontaine A., Trimby P., Harley S., Yang L., Armstrong R. and Cairney J. M. (2016) Deformation-induced trace element redistribution in zircon revealed using atom probe tomography. *Nat. Commun.* **7**, 10490.

Reddy S. M., Timms N. E., Trimby P., Kinny P. D., Buchan C. and Blake K. (2006) Crystal-plastic deformation of zircon: A defect in the assumption of chemical robustness. *Geology* **34**, 257.

Reddy S. M., van Riessen A., Saxey D. W., Johnson T. E., Rickard W. D., Fougerouse D., Fischer S., Prosa T. J., Rice K. P. and Reinhard D. A. (2016) Mechanisms of deformation-induced trace element migration in zircon resolved by atom probe and correlative microscopy. *Geochim. Cosmochim. Acta* **195**, 158–170.

Renne P. R., Balco G., Ludwig K. R., Mundil R. and Min K. (2011) Response to the comment by WH Schwarz et al. on "Joint determination of ^{40}K decay constants and ^{40}Ar*/^{40}K for the Fish Canyon sanidine standard, and improved accuracy for ^{40}Ar/^{39}Ar geochronology" by PR Renne et al. (2010). *Geochim. Cosmochim. Acta* **75**, 5097–5100.

Renne P. R., Swisher C. C., Deino A. L., Karner D. B., Owens T. L. and DePaolo D. J. (1998) Intercalibration of standards, absolute ages and uncertainties in ^{40}Ar/^{39}Ar dating. *Chem. Geol.* **145**, 117–152.

Ryder G., Stoeser D. B., Marvin U. B., Bower J. F. and Wood J. A. (1975) Boulder 1, Station 2, Apollo 17: Petrology and petrogenesis. *The Moon* **14**, 327–357.

Schmitt H. H. (1975) Geological model for Boulder 1 at Station 2, South Massif, Valley of Taurus-Littrow. *The Moon* **14**, 491–504.

Shearer C. K., Elardo S. M., Petro N. E., Borg L. E. and McCubbin F. M. (2015) Origin of the lunar highlands Mg-suite: An integrated petrology, geochemistry, chronology, and remote sensing perspective. *Am. Mineral.* **100**, 294–325.

Sláma J., Košler J., Condon D. J., Crowley J. L., Gerdes A., Hanchar J. M., Horstwood M. S., Morris G. A., Nasdala L. and Norberg N. (2008) Plešovice zircon - a new natural

reference material for U-Pb and Hf isotopic microanalysis. *Chem. Geol.* **249**, 1–35.

Stacey J. S. and Kramers J. D. (1975) Approximation of terrestrial lead isotope evolution by a two-stage model. *Earth Planet. Sci. Lett.* **26**, 207–221.

Takeda H., Mori H. and Miyamoto M. (1982) Comparison of thermal history of orthopyroxenes between Lunar Norites 78236, 72255, and diogenites. *J. Geophys. Res. Solid Earth* **87**, A124.

Thiessen F., Nemchin A. A., Snape J. F., Whitehouse M. J. and Bellucci J. J. (2017) Impact history of the Apollo 17 landing site revealed by U-Pb SIMS ages. *Meteorit. Planet. Sci.* **52**, 584–611.

Timms N. E., Kinny P. D., Reddy S. M., Evans K., Clark C. and Healy D. (2011) Relationship among titanium, rare earth elements, U-Pb ages and deformation microstructures in zircon: Implications for Ti-in-zircon thermometry. *Chem. Geol.* **280**, 33–46.

Utsunomiya S., Palenik C. S., Valley J. W., Cavosie A. J., Wilde S. A. and Ewing R. C. (2004) Nanoscale occurrence of Pb in an Archean zircon. *Geochim. Cosmochim. Acta* **68**, 4679–4686.

Valley J. W., Cavosie A. J., Ushikubo T., Reinhard D. A., Lawrence D. F., Larson D. J., Clifton P. H., Kelly T. F., Wilde S. A. and Moser D. E. (2014) Hadean age for a post-magma-ocean zircon confirmed by atom-probe tomography. *Nat. Geosci.* **7**, 219.

Villa I. M., De Bièvre P., Holden N. and Renne P. (2015) IUPAC-IUGS recommendation on the half life of 87Rb. *Geochim. Cosmochim. Acta* **164**, 382–385.

Watson E. B., Chemiak D. J., Hanchar J. M., Harrison T. M. and Wark D. A. (1997) The incorporation of Pb into zircon. *Chem. Geol.* **141**, 19–31.

Whitehouse M. J., Kumar G. R. and Rimša A. (2014) Behaviour of radiogenic Pb in zircon during ultrahigh-temperature metamorphism: an ion imaging and ion tomography case study from the Kerala Khondalite Belt, southern India. *Contrib. Mineral. Petr.* **168**, 1042.

Whitehouse M. J., Kusiak M. A., Wirth R. and Ravindra Kumar G. R. (2017) Metallic Pb nanospheres in ultra-high temperature metamorphosed zircon from southern India. *Mineral. Petrol.* **111**, 467–474.

Williams I. S., Compston W., Black L. P., Ireland T. R. and Foster J. J. (1984) Unsupported radiogenic Pb in zircon: a cause of anomalously high Pb-Pb, U-Pb and Th-Pb ages. *Contrib. Mineral. Petr.* **88**, 322–327.

Winzer S., Nava D., Lum R., Schuhmann S., Schuhmann P. and Philpotts J. (1975) Origin of 78235, a lunar norite cumulate. *Lunar Planetary Science Conference Proceedings*, 1219–1229.

Wolfe, R. (1974) Interdisciplinary studies of samples from Boulder 1, Station 2, Apollo 17, volume 1.

Wood J. A. (1975) The nature and origin of Boulder 1, Station 2, Apollo 17. *The Moon* **14**, 505–517.

Yang W., Lin Y.-T., Zhang J.-C., Hao J.-L., Shen W.-J. and Hu S. (2012) Precise micrometre-sized Pb-Pb and U-Pb dating with NanoSIMS. *J. Anal. At. Spectrom.* **27**, 479–487.

Zhou Q., Yin Q.-Z., Young E. D., Li X.-H., Wu F.-Y., Li Q.-L., Liu Y. and Tang G.-Q. (2013) SIMS Pb-Pb and U-Pb age determination of eucrite zircons at <5 μm scale and the first 50 Ma of the thermal history of Vesta. *Geochim. Cosmochim. Acta* **110**, 152–175.

Associate editor: Noriko T. Kita